

See discussions, stats, and author profiles for this publication at: <https://www.researchgate.net/publication/231532302>

# Superparamagnetic Ceramic Nanocomposites: Synthesis and Pyrolysis of Ring-Opened Poly(ferrocenylsilanes) inside Periodic Mesoporous Silica

ARTICLE in JOURNAL OF THE AMERICAN CHEMICAL SOCIETY · APRIL 2000

Impact Factor: 12.11 · DOI: 10.1021/ja992006y

---

CITATIONS

89

---

READS

28

7 AUTHORS, INCLUDING:



[Mark J MacLachlan](#)

University of British Columbia - Vancouver

166 PUBLICATIONS 5,275 CITATIONS

SEE PROFILE



[Neil Coombs](#)

University of Toronto

119 PUBLICATIONS 8,570 CITATIONS

SEE PROFILE

# Superparamagnetic Ceramic Nanocomposites: Synthesis and Pyrolysis of Ring-Opened Poly(ferrocenylsilanes) inside Periodic Mesoporous Silica

Mark J. MacLachlan,<sup>†</sup> Madlen Ginzburg,<sup>†</sup> Neil Coombs,<sup>†</sup> Nandyala P. Raju,<sup>‡</sup>  
John E. Greedan,<sup>‡</sup> Geoffrey A. Ozin,<sup>\*,†</sup> and Ian Manners<sup>\*,†</sup>

Contribution from the Department of Chemistry, University of Toronto, 80 St. George Street, Toronto, Ontario, Canada M5S 3H6, and the Brockhouse Institute for Materials Research, McMaster University, Hamilton, Ontario, Canada L8S 4M1

Received June 14, 1999

**Abstract:** [1]Silaferrrocenophanes  $\text{fcSiMe}_2$  (**1**) and  $\text{fcSi}(\text{CH}_2)_3$  (**3**) ( $\text{fc} = \text{Fe}(\eta^5\text{-C}_5\text{H}_4)_2$ ) were incorporated into the well-ordered, hexagonal channels of mesoporous silica (MCM-41). Characterization of the composite materials indicates the presence of ring-opened monomer, oligomer, and polymer, and, in the case of **1**, also free monomer. Polymerization of monomer **1** inside the channels of MCM-41 was demonstrated by DSC. However, in the case of **3** only the ferrocenophane ring was completely opened, and the silacyclobutane ring was mostly intact. When pyrolyzed at 900 °C in a nitrogen atmosphere, the mesoporous silica/ferrocenylsilane composites formed Fe nanoparticles in the ca. 30–40 Å channels of MCM-41. Characterization of the magnetic properties of the product formed when **1** is pyrolyzed in the channels of mesoporous silica indicated that the clusters were superparamagnetic. Magnetization versus field data at 300 K were fit to a sum of two Langevin functions, implying the presence of two distinct magnetic phases. From the magnetization data, the two phases are best described as Fe nanoparticles with diameters of 50–64 Å coated with a thin (ca. 4–6 Å) oxide layer. The product obtained from the pyrolysis of poly(ferrocenylsilane) **2** in the channels of MCM-41 contains much smaller Fe particles than those observed in a pyrolysis of bulk **2**, indicating that the silica channels affect the nucleation and growth of the Fe nanoparticles.

## Introduction

Materials with submicron dimensions (e.g., nanofibers, nanotubes, nanoparticles) represent an exciting new class of materials.<sup>1,2</sup> As a consequence of their tiny size, nanomaterials often display unique physical and chemical properties that are atypical of the bulk material.<sup>2</sup> They are of interest for applications including solid-state lubricants, electronic interconnects in microchip technology, and ceramic reinforcement.<sup>3</sup> In particular, magnetic nanomaterials are attractive as components in magnetic recording media and magnetic fluids.<sup>4</sup> Moreover, studies of the physical properties of magnetic nanoparticles are relevant to understanding the ecological significance of magnetosomes in magnetic bacteria (e.g., *Magnetospirillum magnetotacticum*).<sup>5</sup>

Nanoparticles of a magnetic material with dimensions smaller than that of a single Weiss domain are superparamagnetic.<sup>6,7</sup>

Specifically, the nanoparticles behave as ferromagnets below the blocking temperature ( $T_b$ ) and as giant paramagnets above  $T_b$ . Above  $T_b$ , thermally induced fluctuations result in a random orientation of the magnetic dipoles of the nanoparticles. Superparamagnetic nanoparticles are of interest for use as contrast agents for magnetic resonance imaging (MRI) of biological tissues.<sup>8</sup>

Although nanomaterials are still predominantly prepared by physical methods (e.g., sputtering and molecular beam epitaxy), there is a desire to prepare the materials by chemical techniques. Chemical routes are generally simpler and less expensive and have the advantages of improved stoichiometric control and intimate mixing.<sup>1</sup> Numerous methods for the preparation of metal nanoparticles have been reported, including reduction of metal salts and thermolysis or sonication of organometallic complexes.<sup>2,6,7</sup> Ideally, the fabrication technique should exert control over the particle size, distribution, and morphology. By forming the nanoparticles inside templates such as zeolites, micelles, block copolymers, porous alumina, and polycarbonate

<sup>†</sup> University of Toronto.

<sup>‡</sup> McMaster University.

(1) Ozin, G. A. *Adv. Mater.* **1992**, *4*, 612.

(2) For example, see: (a) Special issue of *Chem. Mater.* **1996**, *8* (8). (b) Special issue of *New J. Chem.* **1998**, *22* (7). (c) Special issue of *New J. Chem.* **1998**, *22* (11). (d) Steffens, K. L.; Zachariah, M. R.; DuFaux, D. P.; Axelbaum, R. L. *Chem. Mater.* **1996**, *8*, 1871. (e) Dagani, R. *Chem. Eng. News* **1992**, *70* (47), 18. (f) Gehr, R. J.; Boyd, R. W. *Chem. Mater.* **1996**, *8*, 1807. (g) Gleiter, H. *Adv. Mater.* **1992**, *4*, 474. (h) Whetten, R. L.; Khoury, J. T.; Alvarez, M. M.; Murthy, S.; Vezmar, I.; Wang, Z. L.; Stephens, P. W.; Cleveland, C. L.; Luedtke, W. D.; Landman, U. *Adv. Mater.* **1996**, *8*, 428.

(3) See, for example: (a) Beaucage, G., Ed. *Nanostructured Powders and Their Industrial Applications*; MRS: Warrendale, PA, 1998. (b) Jena, P., Ed. *Nanostructured Materials*; Nova Science: New York, 1996.

(4) (a) Spiliotis, D. E. *J. Magn. Magn. Mater.* **1999**, *193*, 29. (b) Hadjipanayis, G. C.; Prinz, G. A., Eds. *Science and Technology of Nanostructured Magnetic Materials*; Plenum Press: New York, 1991. (c) Rosenweig, R. E. *Ferrohydrodynamics*; Cambridge University Press: Cambridge, 1985.

(5) Matsunaga, T.; Takeyama, H. *Supramol. Sci.* **1998**, *5*, 391.

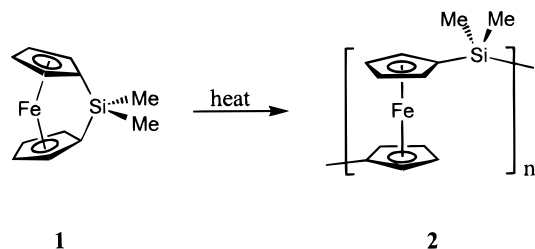
(6) Leslie-Pelecky, D. L.; Rieke, R. D. *Chem. Mater.* **1996**, *8*, 1770.

(7) See, for example (a) Chhabra, V.; Ayyub, P.; Chattopadhyay, S.; Maitra, A. N. *Mater. Lett.* **1996**, *26*, 21. (b) Choukroun, R.; de Caro, D.; Matéo, S.; Amiens, C.; Chaudret, B.; Snoeck, E.; Respaud, M. *New J. Chem.* **1998**, *22*, 1295. (c) de Caro, D.; Ely, T. O.; Mari, A.; Chaudret, B.; Snoeck, E.; Respaud, M.; Broto, J.-M.; Fert, A. *Chem. Mater.* **1996**, *8*, 1987. (d) Gonsalves, K. E.; Carlson, G.; Benaissa, M.; Jose-Yacamán, M.; Kim, D. Y.; Kumar, J. J. *Mater. Chem.* **1997**, *7*, 703. (e) Pascal, C.; Pascal, J. L.; Favier, F.; Moubassim, M. L. E.; Payen, C. *Chem. Mater.* **1999**, *11*, 141. (f) Cao, X.; Koltypin, Y.; Katabi, G.; Prozorov, R.; Felner, I.; Gedanken, A. *J. Mater. Chem.* **1997**, *7*, 1007. (g) Letellier, D.; Sandre, O.; Ménager, C.; Cabuil, V.; Laverne, M. *Mater. Sci. Eng. C* **1997**, *5*, 153. (h) Bødker, F.; Mørup, S. *Hyperfine Interact.* **1994**, *93*, 1421.

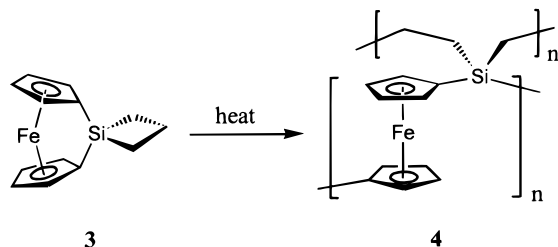
(8) Clément, O.; Siauve, N.; Lewin, M.; de Kerviler, E.; Cuénod, C.-A.; Frija, G. *Biomed. Pharmacother.* **1998**, *52*, 51.

membranes, greater control over the particle-size distribution can be obtained.<sup>6,9</sup>

In 1992, Kresge et al. reported the synthesis of mesoporous silica, MCM-41, possessing ordered channels arranged in a hexagonal lattice.<sup>10</sup> With uniform channel sizes readily varied between 20 and 100 Å in diameter, this material is well-suited to be a host for novel nanomaterials. Indeed, researchers have reported a variety of nanochemistry within the channels and MCM-41 has been used to template nanosized rhodium oxide particles.<sup>11,12</sup>



We have been exploring the ring-opening polymerization (ROP) of [1]silaferrocenophanes (e.g., **1**) which yields soluble, high-molecular-weight poly(ferrocenylsilanes) **2**.<sup>13,14</sup> When pyrolyzed, polymer **2** forms a ferromagnetic ceramic in 22% yield that shows hysteresis in its field-dependent magnetization curve at room temperature.<sup>15</sup> To improve the ceramic yield, we have been exploring the use of spirocyclic [1]ferrocenophane **3** to cross-link poly(ferrocenes).<sup>16,17</sup> The cross-linked network **4** formed from the homopolymer of **3** can be pyrolyzed at 600 °C to give a shaped superparamagnetic ceramic in 90% yield.<sup>17c</sup>



(9) (a) Hulteen, J. C.; Martin, C. R. *J. Mater. Chem.* **1997**, 7, 1075. (b) Martin, C. R. *Acc. Chem. Res.* **1995**, 28, 61. (c) Martin, C. R. *Chem. Mater.* **1996**, 8, 1739. (d) Schöllhorn, R. *Chem. Mater.* **1996**, 8, 1747. (e) Frisch, H. L.; Mark, J. E. *Chem. Mater.* **1996**, 8, 1735.

(10) (a) Kresge, C. T.; Leonowicz, M. E.; Roth, W. J.; Vartuli, J. C.; Beck, J. S. *Nature* **1992**, 359, 710. (b) Beck, J. S.; Vartuli, J. C.; Roth, W. J.; Leonowicz, M. E.; Kresge, C. T.; Schmitt, K. D.; Chu, C. T.-W.; Olson, D. H.; Sheppard, E. W.; McCullen, S. B.; Higgins, J. B.; Schlenker, J. L. *J. Am. Chem. Soc.* **1992**, 114, 10834.

(11) (a) Ozin, G. A.; Chomski, E.; Khushalani, D.; MacLachlan, M. J. *Curr. Opin. Colloid Interface Sci.* **1998**, 3, 181. (b) Moller, K.; Bein, T. *Chem. Mater.* **1998**, 10, 2950.

(12) Mulukutla, R. S.; Asakura, K.; Namba, S.; Iwasawa, Y. *Chem. Commun.* **1998**, 1425.

(13) Foucher, D. A.; Tang, B.-Z.; Manners, I. *J. Am. Chem. Soc.* **1992**, 114, 6246.

(14) (a) Manners, I. *Adv. Organomet. Chem.* **1995**, 37, 131. (b) Manners, I. *Can. J. Chem.* **1998**, 76, 371.

(15) (a) Tang, B.-Z.; Peterson, R.; Foucher, D. A.; Lough, A.; Coombs, N.; Sodhi, R.; Manners, I. *J. Chem. Soc., Chem. Commun.* **1993**, 523. (b) Petersen, R.; Foucher, D. A.; Tang, B.-Z.; Lough, A.; Raju, N. P.; Greedan, J. E.; Manners, I. *Chem. Mater.* **1995**, 7, 2045.

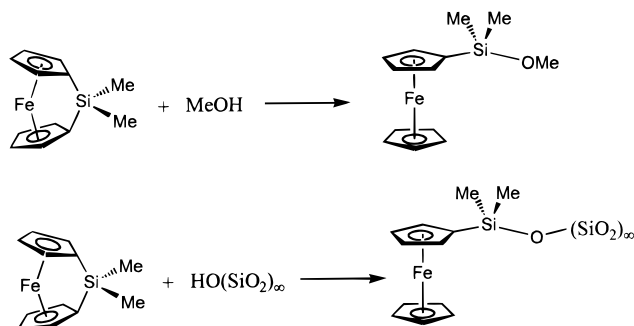
(16) MacLachlan, M. J.; Lough, A. J.; Geiger, W. E.; Manners, I. *Organometallics* **1998**, 17, 1873.

(17) (a) MacLachlan, M. J.; Lough, A. J.; Manners, I. *Macromolecules* **1996**, 29, 8562. (b) Kulbaba, K.; MacLachlan, M. J.; Manners, I. Manuscript in preparation. (c) MacLachlan, M. J.; Ginzburg, M.; Coombs, N.; Coyle, T. W.; Raju, N. P.; Greedan, J. E.; Ozin, G. A.; Manners, I. *Science* **2000**, 287, 1460.

Pyrolysis of poly(ferrocenylsilanes) in MCM-41 is desirable as a route to control the particle size of nanomaterials.<sup>18</sup> Whereas large Fe particles result from bulk pyrolysis of poly(ferrocenylsilanes),<sup>15</sup> smaller particles may form in the channels of MCM-41, as a consequence of restrictions from the channel dimensions. This size control has already been employed in the synthesis of a few nanomaterials.<sup>11</sup> Bein and co-workers have encapsulated conducting polyaniline and graphitic nanowires inside MCM-41.<sup>19</sup> Mallouk, Ozin, and co-workers have prepared extractable polyphenol-formaldehyde nanofibers inside MCM-41.<sup>20</sup> Chomski et al. impregnated MCM-41 with disilane to form luminescent silicon clusters in the channels.<sup>21</sup>

The reaction of MeOH with [1]silaferrocenophane **1** leads to ring-opening OH addition to the Si-Cp bond of **1** to give  $\text{FcSiMe}_2\text{OMe}$  ( $\text{Fc} = \text{Fe}(\eta^5\text{-C}_5\text{H}_4)(\eta^5\text{-C}_5\text{H}_5)$ ) as shown in Scheme 1.<sup>22</sup> This methodology has subsequently been used to modify

### Scheme 1



amorphous and mesoporous silica, anchoring **1** to the reactive  $\equiv\text{SiOH}$  sites present on the surface of the silica.<sup>22,23</sup> O'Brien et al. treated MCM-41 with a pentane solution of **1** to obtain a maximum loading of 65 wt % **1** in the hydrated host.<sup>23</sup> We have recently reported preliminary studies of the ROP of **1** inside mesoporous silica and the subsequent pyrolysis to afford a composite with Fe nanoparticles inside the channels of MCM-41.<sup>24</sup>

In this paper, we report full details of our studies of the synthesis and characterization of ceramic composites made from mesoporous silica containing **1** or **3**. Furthermore, studies of the pyrolysis, including the first magnetization data for iron nanoparticles inside mesoporous silica, are reported.

### Experimental Section

**General Comments.** [1]Silaferrocenophanes **1** and **3** were prepared by literature methods.<sup>13,16</sup> They were both recrystallized and then sublimed multiple times prior to use. Well-ordered MCM-41 (CPM-

(18) Poly(ferrocene) block copolymers provide an alternative methodology for accessing nanostructures via phase separation in the solid state and aggregation in block selective solvents. See: (a) Massey, J. A.; Power, K. N.; Winnik, M. A.; Manners, I. *Adv. Mater.* **1998**, 10, 1559. (b) Manners, I. *Chem. Commun.* **1999**, 857. (c) Manners, I. *Pure Appl. Chem.* **1999**, 71, 1471.

(19) (a) Wu, C.-G.; Bein, T. *Science* **1994**, 264, 1757. (b) Wu, C.-G.; Bein, T. *Chem. Mater.* **1994**, 6, 1109. (c) Wu, C.-G.; Bein, T. *Science* **1994**, 266, 1013.

(20) Johnson, S. A.; Khushalani, D.; Coombs, N.; Mallouk, T. E.; Ozin, G. A. *J. Mater. Chem.* **1998**, 7, 13.

(21) Chomski, E.; Dag, Ö.; Kuperman, A.; Coombs, N.; Ozin, G. A. *Chem. Vap. Deposition* **1996**, 2, 8.

(22) Fischer, A. B.; Kinney, J. B.; Staley, R. H.; Wrighton, M. S. *J. Am. Chem. Soc.* **1979**, 101, 6501.

(23) (a) O'Brien, S.; Tudor, J.; Barlow, S.; Drewitt, M. J.; Heyes, S. J.; O'Hare, D. *Chem. Commun.* **1997**, 641. (b) O'Brien, S.; Keates, J. M.; Barlow, S.; Drewitt, M. J.; Payne, B. R.; O'Hare, D. *Chem. Mater.* **1998**, 10, 4088.

(24) MacLachlan, M. J.; Aroca, P.; Coombs, N.; Manners, I.; Ozin, G. A. *Adv. Mater.* **1998**, 10, 144.

MCM, ODA-MCM) was prepared by a literature method (base-catalyzed condensation of  $\text{Si}(\text{OEt})_4$  using cetylpyridinium (CPM) chloride and octadecyltrimethylammonium (ODA) chloride, respectively, as the structure-directing template.<sup>25</sup> Calcination under air at 540 °C resulted in template removal. Reflectance UV-vis/near-IR spectra were obtained on a Perkin-Elmer Lambda 900 spectrometer. Solid-state NMR, PXRD, TEM, ED, SQUID magnetometry, pyrolysis, and DSC experiments were performed as reported in previous publications.<sup>15,24</sup> IR spectra were collected as KBr pellets on a Perkin-Elmer Paragon 500 FT-IR spectrometer. Fe analyses were obtained from Quantitative Technologies Inc. (Whitehouse, NJ). Samples were digested in a mixture of perchloric, sulfuric, and nitric acids and then analyzed by ICP.

**Synthesis of MCM-41/ $\text{fcSiMe}_2$  Composites 5.** Samples of the ferrocenylsilane/silica composite were prepared with different loadings of **1** and different pore sizes of MCM-41. To prepare composite **5a**, 292 mg of ODA-MCM in a Schlenk tube was heated under vacuum (ca.  $10^{-4}$  Torr) to 250 °C over 4 h and held there for 2 h. The sample was cooled to room temperature and then transferred to a glovebox. Monomer **1** (97 mg, 0.40 mmol) was added and mixed with the silica. After standing under vacuum for 3 days, the powder appeared homogeneous and orange. The powder was transferred to a sublimator and kept under dynamic vacuum (ca.  $10^{-3}$  Torr) at room temperature for 24 h. The absence of any sublimate indicated that there was no excess monomer in the sample. Composite **5b** was prepared by the same procedure using 310 mg of ODA-MCM and 170 mg of **1**; no excess monomer was sublimed from the product. Composite **5c** was prepared by the same procedure using 424 mg of ODA-MCM and 315 mg of **1**; a small amount of excess monomer was removed by sublimation. Composite **5d** was prepared by the same procedure using 1.070 g of CPM-MCM and 1.150 g of **1**; some excess monomer was removed by sublimation.

**Data for 5a.** Yellow powder. PXRD:  $d = 42.7$  (MCM-41,  $d_{100}$ ), 24.7 (MCM-41,  $d_{110}$ ), 21.4 (MCM-41,  $d_{200}$ ), 16.1 (MCM-41,  $d_{210}$ ), 6.3 (br halo,  $[\text{fcSiMe}_2]_n$ ), 4 (br halo,  $\text{SiO}_2$ ) Å.  $^1\text{H}$  MAS NMR (spin rate 2.8 kHz, recycle delay 2 s):  $\delta = 0.0$  ( $\text{CH}_3$ ), 0.8 ( $\text{CH}_3$ ), 1.2 ( $\text{CH}_3$ ), 1.8 ( $\text{SiOH}$ ), 4.0 (br, Cp) ppm.  $^{13}\text{C}$  CP-MAS NMR (spin rate 10.5 kHz, recycle delay 2 s, contact time 1 ms):  $\delta = 0.6$  ( $\text{CH}_3$ ), 68.0 (Cp), 72.2 (Si-Cp) ppm.  $^{29}\text{Si}$  CP-MAS NMR (spin rate 5 kHz, recycle delay 10 s, contact time 3 ms):  $\delta = -108$  (br,  $\text{SiO}_2$ ),  $-6.5$  ( $[\text{fcSiMe}_2]_n$ ), 6.4 (CpSiMe<sub>2</sub>O) ppm. UV-vis/near-IR:  $\lambda = 2430\text{w}$ , 2389w, 2317w, 1759w, 1718w, 1665m, 627w, 459s, 336w, 262vs nm. Fe analysis: 3.45%.

**Data for 5b.** Yellow powder. PXRD:  $d = 43.1$  (MCM-41,  $d_{100}$ ), 24.8 (MCM-41,  $d_{110}$ ), 21.6 (MCM-41,  $d_{200}$ ), 16.0 (MCM-41,  $d_{210}$ ), 6.3 (br halo,  $[\text{fcSiMe}_2]_n$ ), 4 (br halo,  $\text{SiO}_2$ ) Å.  $^1\text{H}$  MAS NMR (9 kHz spin rate, 10 s recycle delay):  $\delta = 0.2$  ( $\text{CH}_3$ ), 1.7 (OH), 4.0 (Cp) ppm.  $^{13}\text{C}$  CP-MAS NMR (9 kHz spin rate, 2 s recycle delay, 1 ms contact time):  $\delta = -0.4$  ( $\text{CH}_3$ ), 68.1 (Cp), 71.6 (Si-Cp) ppm.

**Data for 5c.** Yellow-orange powder. PXRD:  $d = 42.7$  (MCM-41,  $d_{100}$ ), 24.4 (MCM-41,  $d_{110}$ ), 21.2 (MCM-41,  $d_{200}$ ), 15.9 (MCM-41,  $d_{210}$ ), 6.3 (br halo,  $[\text{fcSiMe}_2]_n$ ), 4 (br halo,  $\text{SiO}_2$ ) Å.  $^1\text{H}$  MAS NMR (7 kHz spin rate, 10 s recycle delay):  $\delta = 0.2$  ( $\text{CH}_3$ ), 1.0 ( $\text{CH}_3$ ), 4.0 (Cp) ppm.  $^{13}\text{C}$  CP-MAS NMR (10 kHz spin rate, 2 s recycle delay, 1 ms contact time):  $\delta = 0.4$  (br,  $\text{CH}_3$ ), 15–50 (*ipso*-Cp), 68.2 (Cp), 72.0 (Si-Cp) ppm.  $^{29}\text{Si}$  CP-MAS NMR (5 kHz spin rate, 2 s recycle delay, 3 ms contact time):  $\delta = -107$  (br,  $\text{SiO}_2$ ),  $-6.8$  ( $[\text{fcSiMe}_2]_n$ ), 0.3, 6.9 (CpSiMe<sub>2</sub>O) ppm. UV-vis/near-IR:  $\lambda = 2430\text{w}$ , 2392w, 2314w, 1762w, 1714w, 1666m, 1135w, 459s, 337m, 266vs nm. IR (KBr):  $\bar{\nu} = 3101\text{w}$  ( $\nu\text{C-H}$ ), 2963w ( $\nu\text{C-H}$ ), 2903w ( $\nu\text{C-H}$ ), 1422w, 1381w, 1367w, 1249s, 1167m, 1083vs ( $\nu\text{Si-O}$ ), 901m, 818s, 796m, 666m, 452s  $\text{cm}^{-1}$ . Fe analysis: 5.41%.

**Data for 5d.** Yellow-orange powder. PXRD:  $d = 37.3$  (MCM-41,  $d_{100}$ ), 21.7 (MCM-41,  $d_{110}$ ), 18.7 (MCM-41,  $d_{200}$ ), 6.3 (br halo,  $[\text{fcSiMe}_2]_n$ ) Å, 4 (br halo,  $\text{SiO}_2$ ) Å.  $^1\text{H}$  MAS NMR (1.85 kHz spin rate, 2 s recycle delay):  $\delta = -0.5$  ( $\text{CH}_3$ ), 1.7 ( $\text{CH}_3$ ), 4.0 (Cp) ppm.  $^{13}\text{C}$  CP-MAS NMR (7 kHz spin rate, 2 s recycle delay, 1 ms contact time):  $\delta = 0.2$  ( $\text{CH}_3$ ), 68.3 (Cp), 72.2 (Si-Cp) ppm.  $^{29}\text{Si}$  CP-MAS

NMR (5 kHz spin rate, 10 s recycle delay, 3 ms contact time):  $\delta = -107$  (br,  $\text{SiO}_2$ ),  $-6.6$  ( $[\text{fcSiMe}_2]_n$ ), 0.1, 7.6 (CpSiMe<sub>2</sub>O) ppm. UV-vis/near-IR:  $\lambda = 2430\text{w}$ , 2392w, 2316w, 1762w, 1714w, 1666m, 1205w, 1135w, 458s, 335m, 268vs nm.

**Polymerization of 1 within the Channels of MCM-41 To Give Composite 6.** The fully loaded composite **5c** (ca. 200 mg) was placed in a Schlenk flask and heated under  $\text{N}_2$  to 140 °C in an oil bath for 4 h. A color change from orange to yellow was observed, and a small amount of ferrocene (identified by  $^1\text{H}$  NMR) sublimed onto the colder part of the glassware.

**Data for 6.** PXRD:  $d = 41.8$  (MCM-41,  $d_{100}$ ), 24.2 (MCM-41,  $d_{110}$ ), 21.1 (MCM-41,  $d_{200}$ ), 15.9 (MCM-41,  $d_{210}$ ), 6.3 (br halo,  $[\text{fcSiMe}_2]_n$ ), 4 (br halo,  $\text{SiO}_2$ ) Å.  $^1\text{H}$  MAS NMR (10 kHz spin rate, 10 s recycle delay):  $\delta = 0.1$  ( $\text{CH}_3$ ), 1.6 (OH), 3.8 (Cp) ppm.  $^{13}\text{C}$  CP-MAS NMR (10 kHz spin rate, 2 s recycle delay, 1 ms contact time):  $\delta = 0.0$  ( $\text{CH}_3$ ), 68.5 (Cp), 71 (sh, Si-Cp) ppm.  $^{29}\text{Si}$  CP-MAS NMR (79.50 MHz, 6 kHz spin rate, 10 s recycle delay, 5 ms contact time):  $\delta = -108$  (br,  $\text{SiO}_2$ ),  $-6.7$  ( $[\text{fcSiMe}_2]_n$ ), 0.2, 7.2 (CpSiMe<sub>2</sub>O) ppm. UV-vis/near-IR:  $\lambda = 2430\text{w}$ , 2395w, 2318w, 1666m, 1335w, 457s, 335m, 266vs nm. IR (KBr):  $\lambda = 3436\text{w}$ , br ( $\nu\text{OH}$ ), 3097m ( $\nu\text{C-H}$ ), 2967m ( $\nu\text{C-H}$ ), 2929m ( $\nu\text{C-H}$ ), 2874m ( $\nu\text{C-H}$ ), 1420w, 1384w, 1249s, 1166m, 1083s, br ( $\nu\text{Si-O}$ ), 904w, 818m, 700w, 679w, 568w, 451m  $\text{cm}^{-1}$ .

**Synthesis of MCM-41/ $\text{fcSi}(\text{CH}_2)_3$  Composite 7.** CPM-MCM (1.32 g) was heated overnight in a Schlenk tube at 100 °C, raised to 200 °C in 1 h, and then held at 200 °C for 2 h under dynamic vacuum (ca.  $10^{-4}$  Torr). After the Schlenk tube was cooled to room temperature, the silica was transferred to a glovebox, where 1.38 g (5.43 mmol) of spirocyclic [1]ferrocenophane **3** was added. The Schlenk tube was then placed under static vacuum (ca.  $10^{-4}$  Torr) for 5 days at room temperature. The color of the mixture was observed to change from a white and red mixture to a white and orange powder in 1 day and to a homogeneous orange powder after 3 days. Excess monomer was removed by sublimation at 45 °C under dynamic vacuum for 6 days.

**Data for 7.** Yellow powder. PXRD:  $d = 36.5$  (MCM-41,  $d_{100}$ ), 21.5 (MCM-41,  $d_{110}$ ), 18.6 (MCM-41,  $d_{200}$ ), 14.1 (MCM-41,  $d_{210}$ ), 6 (br halo,  $[\text{fcSi}(\text{CH}_2)_3]_n$ ), 4 (br halo,  $\text{SiO}_2$ ) Å.  $^1\text{H}$  MAS NMR (5 kHz spin rate, 1 s recycle delay):  $\delta = 0.2$  ( $\text{CH}_2$ ), 4.1 (Cp) ppm.  $^{13}\text{C}$  CP-MAS NMR (5 kHz spin rate, 10 s recycle delay, 5 ms contact time):  $\delta = 14.6$  ( $\text{CH}_2$ ), 17.8 ( $\text{CH}_2$ ), 68.3 (Cp), 72.2 (Si-Cp) ppm.  $^{29}\text{Si}$  CP-MAS NMR (5 kHz spin rate, 10 s recycle delay, 5 ms contact time):  $\delta = -107$  (br,  $\text{SiO}_2$ ), 8.8 ( $\text{R}_3\text{SiO}$ ) ppm. UV-vis:  $\lambda = 453\text{s}$ , 270vs nm. IR (KBr):  $\bar{\nu} = 3437\text{m}$ , br ( $\nu\text{O-H}$ ), 3097w ( $\nu\text{C-H}$ ), 2967m ( $\nu\text{C-H}$ ), 2929m ( $\nu\text{C-H}$ ), 2874w ( $\nu\text{C-H}$ ), 1636w, 1420w, 1384w, 1249s, 1166m, 1083vs ( $\nu\text{Si-O}$ ), 904w, 818m, 700m, 679m, 568m, 451s  $\text{cm}^{-1}$ . Fe analysis: 4.28%.

**Polymerization of 3 within the Channels of MCM-41 To Give Composite 8.** A sample of **7** in a Schlenk flask was heated to 280 °C in 1 h and held at 280 °C for 4 h under  $\text{N}_2$ . The solid changed color from yellow-orange to yellow-brown.

**Data for 8.** PXRD:  $d = 36.3$  (MCM-41,  $d_{100}$ ), 21.3 (MCM-41,  $d_{110}$ ), 18.6 (MCM-41,  $d_{200}$ ), 6.3 (br halo,  $[\text{fcSi}(\text{CH}_2)_3]_n$ ), 4 (br halo,  $\text{SiO}_2$ ) Å.  $^{13}\text{C}$  CP-MAS NMR (6 kHz spin rate, 2 s recycle delay, 5 ms contact time):  $\delta = 16.9$  ( $\text{CH}_2$ ), 68.4 (Cp), 72 (Si-Cp) ppm.  $^{29}\text{Si}$  CP-MAS NMR (4 kHz spin rate, 10 s recycle delay, 5 ms contact time):  $\delta = -107$  (br,  $\text{SiO}_2$ ),  $-58$  (w, br,  $\text{RSiO}_3$ ),  $-25$  (br,  $\text{R}_2\text{SiO}_2$ ), 5, 9 ( $\text{R}_3\text{SiO}$ ) ppm. UV-vis/near-IR:  $\lambda = 1916\text{w}$ , 1768w, 1666m, 460s, 270vs nm.

**Pyrolysis of Composites 5a–d.** Sample **5a** (222 mg) was placed in a small preweighed quartz boat. The quartz boat was placed inside a tube furnace and purged with a  $\text{N}_2$  atmosphere. Under a slow flow of  $\text{N}_2$  (ca. 50 mL  $\text{min}^{-1}$ ), the temperature was raised from 25 to 900 °C in 8 h and was held at 900 °C for 2 h. The product was a brown powder (yield 190 mg, 86%). During the pyrolysis, a small amount of ferrocene (identified by  $^1\text{H}$  NMR) condensed on the cold part of the quartz tube. Samples **5b–d** were pyrolyzed under the same conditions to give ceramics **9b–d**, respectively.

**Data for 9a.** Ceramic yield: 86%. Brown powder. PXRD:  $d = 40.8$  (MCM-41,  $d_{100}$ ), 23.5 (MCM-41,  $d_{110}$ ), 20.4 (MCM-41,  $d_{200}$ ), 15.5 (MCM-41,  $d_{210}$ ), 4 (br halo,  $\text{SiO}_2$ ) Å.

**Data for 9b.** Ceramic yield: 80%. Fine black powder. PXRD:  $d = 40.8$  (MCM-41,  $d_{100}$ ), 23.6 (MCM-41,  $d_{110}$ ), 20.5 (MCM-41,  $d_{200}$ ), 4 (br halo,  $\text{SiO}_2$ ) Å.

(25) Khushalani, D.; Kuperman, A.; Coombs, N.; Ozin, G. A. *Chem. Mater.* **1996**, *8*, 2188.



**Table 1.** Pyrolysis Temperature, Duration, and Ceramic Yields for **10a–i**

sample	temp (°C)	time (h)	yield, %
<b>10a</b>	500	6	78
<b>10b</b>	600	6	81
<b>10c</b>	800	6	84
<b>10d</b>	900	6	80
<b>10e</b>	1000	6	79
<b>10f</b>	1000	6	77
<b>10g</b>	1000	1	85
<b>10h</b>	1000	24	73
<b>10i</b>	900	2 <sup>a</sup>	76

<sup>a</sup> Ramp to 900 °C in 8 h (for comparison with ceramics **9a–d**).

**Data for 9c.** Ceramic yield: 75%. Brown-black powder. PXRD:  $d = 41.5$  (MCM-41,  $d_{100}$ ), 23.9 (MCM-41,  $d_{110}$ ), 20.8 (MCM-41,  $d_{200}$ ), 15.7 (MCM-41,  $d_{210}$ ), 4 (br halo, SiO<sub>2</sub>), 2.0 (br halo, Fe) Å.

**Data for 9d.** Ceramic yield: 69%. Black powder. PXRD:  $d = 33.0$  (MCM-41,  $d_{100}$ ), 20.0 (MCM-41,  $d_{110}$ ), 17.5 (MCM-41,  $d_{200}$ ), 4 (br halo, SiO<sub>2</sub>), 2.02 (α-Fe,  $d_{110}$ ) Å.

**Pyrolysis of Composite 7.** Ceramic **10a** was prepared from the pyrolysis of **7** at 500 °C. A sample of **7** (206 mg) was placed in a quartz boat inside a tube furnace. The atmosphere was then purged with nitrogen. Under a slow flow of N<sub>2</sub> (ca. 50 mL min<sup>-1</sup>), the sample was heated from room temperature to 500 °C in 4 h and maintained at 500 °C for 6 h. After cooling naturally to room temperature, the sample was weighed. Ceramic **10a** appeared as a light brown powder (161 mg, 78% yield). Ceramics **10b–e** were prepared by an identical procedure starting with 200–300 mg of **7**, but the pyrolysis temperature and time were varied as listed in Table 1. Ceramics **10d,f–i** were prepared using a different sample of composite **7**, one prepared under identical conditions.

**Data for 10a.** Light brown powder. PXRD:  $d = 37.2$  (MCM-41,  $d_{100}$ ), 21.3 (MCM-41,  $d_{110}$ ), 18.5 (MCM-41,  $d_{200}$ ), 4 (br halo, SiO<sub>2</sub>) Å.

**Data for 10b.** Dark brown powder. PXRD:  $d = 37.0$  (MCM-41,  $d_{100}$ ), 21.5 (MCM-41,  $d_{110}$ ), 18.6 (MCM-41,  $d_{200}$ ), 4 (br halo, SiO<sub>2</sub>), 2.2 (br halo, Fe) Å.

**Data for 10c.** Black powder. PXRD:  $d = 36.7$  (MCM-41,  $d_{100}$ ), 21.0 (MCM-41,  $d_{110}$ ), 18.4 (MCM-41,  $d_{200}$ ), 4 (br halo, SiO<sub>2</sub>), 2.1 (br halo, Fe) Å.

**Data for 10d.** Black powder. PXRD:  $d = 35.1$  (MCM-41,  $d_{100}$ ), 20.4 (MCM-41,  $d_{110}$ ), 17.8 (MCM-41,  $d_{200}$ ), 4 (br halo, SiO<sub>2</sub>), 2.1 (br halo, Fe) Å.

**Data for 10e.** Black powder. PXRD:  $d = 35.3$  (MCM-41,  $d_{100}$ ), 20.6 (MCM-41,  $d_{110}$ ), 17.9 (MCM-41,  $d_{200}$ ), 4 (br halo, SiO<sub>2</sub>), 2.52 (Fe<sub>3</sub>O<sub>4</sub>,  $d_{311}$ ), 2.08 (γ-Fe,  $d_{111}$ ), 2.03 (α-Fe,  $d_{110}$ ) Å.

**Data for 10f.** Black powder. PXRD:  $d = 34.4$  (MCM-41,  $d_{100}$ ), 20.1 (MCM-41,  $d_{110}$ ), 17.3 (MCM-41,  $d_{200}$ ), 4 (br halo, SiO<sub>2</sub>), 2.52 (Fe<sub>3</sub>O<sub>4</sub>,  $d_{311}$ ), 2.08 (γ-Fe,  $d_{111}$ ), 2.03 (α-Fe,  $d_{110}$ ) Å.

**Data for 10g.** Black powder. PXRD:  $d = 35.0$  (MCM-41,  $d_{100}$ ), 20.5 (MCM-41,  $d_{110}$ ), 17.7 (MCM-41,  $d_{200}$ ), 4 (br halo, SiO<sub>2</sub>), 2.5 (br halo, Fe<sub>3</sub>O<sub>4</sub>,  $d_{311}$ ), 2.07 (γ-Fe,  $d_{111}$ ), 2.02 (α-Fe,  $d_{110}$ ), 1.79 (γ-Fe,  $d_{200}$ ) Å.

**Data for 10h.** Gray powder. PXRD: 4.25 (quartz,  $d_{100}$ ), 4.04 (cristobalite,  $d_{101}$ ), 4 (br halo, SiO<sub>2</sub>), 3.34 (quartz,  $d_{101}$ ), 2.96 (Fe<sub>3</sub>O<sub>4</sub>,  $d_{220}$ ), 2.52 (Fe<sub>3</sub>O<sub>4</sub>,  $d_{311}$ ), 2.45 (quartz,  $d_{110}$ ), 2.28 (quartz,  $d_{102}$ ), 2.23 (quartz,  $d_{111}$ ), 2.12 (quartz,  $d_{200}$ ), 2.06 (γ-Fe,  $d_{111}$ ), 2.02 (α-Fe,  $d_{110}$ ), 1.98 (quartz,  $d_{201}$ ), 1.82 (quartz,  $d_{112}$ ), 1.79 (Fe<sub>3</sub>O<sub>4</sub>,  $d_{220}$ ), 1.67 (quartz,  $d_{202}$ ), 1.66 (quartz,  $d_{103}$ ), 1.54 (quartz,  $d_{211}$ ), 1.45 (quartz,  $d_{113}$ ) Å.

**Data for 10i.** Black powder. PXRD:  $d = 35.4$  (MCM-41,  $d_{100}$ ), 20.6 (MCM-41,  $d_{110}$ ), 17.8 (MCM-41,  $d_{200}$ ), 2.53 (Fe<sub>3</sub>O<sub>4</sub>, br  $d_{311}$ ), 2.1 (br halo, Fe) Å.

**Control Samples.** A control sample of monomer **1** on amorphous silica was prepared as follows: Hi-sil (synthetic precipitated silica, 322 mg) was heated in a Schlenk tube under vacuum (ca. 10<sup>-4</sup> Torr) to 250 °C over 4 h and held there for 2 h. Monomer **1** (134 mg; 0.55 mmol) was then added, and the mixture was placed under static vacuum for 4 days. The resulting orange powder was transferred to a sublimator and kept under dynamic vacuum (ca. 10<sup>-3</sup> Torr) at room temperature overnight. Excess monomer was sublimed off to leave a yellow powder.

**Table 2.** Summary of Magnetization Parameters for **9b–d** from Fitting to the Langevin Function

	<b>9b</b>	<b>9c</b>	<b>9d</b>
data points	34	23	31
$R^2$	0.9995	0.9997	0.9993
$\chi^2$	0.021	0.0032	0.067
$M_S$ (emu g <sup>-1</sup> )	0.66(2)	0.52(2)	1.84(7)
$\mu_S/kT$ (G)	0.00051(2)	0.00047(2)	0.00103(4)
$M_L$ (emu g <sup>-1</sup> )	0.63(2)	0.50(2)	1.44(7)
$\mu_L/kT$ (G)	0.0028(1)	0.0027(1)	0.0057(4)

Subsequent pyrolysis of 150 mg of this composite at 900 °C (8 h ramp, held for 2 h) gave a light gray powder **11** (97 mg, 65% yield).

Control sample **12** was prepared by making a physical mixture of 191 mg of CPM-MCM and 48 mg (24 wt %) of poly(ferrocenylsilane). Subsequent pyrolysis of 146 mg of **12** under N<sub>2</sub> (ramp to 900 °C in 8 h and holding at 900 °C for 2 h) gave ceramic **13** as a dark gray powder (127 mg, 87% yield). Composite **14** was prepared by mixing 297 mg of CPM-MCM and 74 mg (20 wt %) of cross-linked polymer **4**. Subsequent pyrolysis of **14** (177 mg) under N<sub>2</sub> afforded light gray ceramic **15** (162 mg; 92% yield). The polymers were finely ground before use, and the mixture was lightly ground.

**Data for 11.** Gray-white powder. 4 (br halo, SiO<sub>2</sub>) Å.

**Data for 12.** Heterogeneous orange and white powder. PXRD:  $d = 39.1$  (MCM-41,  $d_{100}$ ), 22.3 (MCM-41,  $d_{110}$ ), 19.3 (MCM-41,  $d_{200}$ ) Å.

**Data for 13.** Gray powder. PXRD:  $d = 37.2$  (MCM-41,  $d_{100}$ ), 21.3 (MCM-41,  $d_{110}$ ), 18.3 (MCM-41,  $d_{200}$ ), 4 (br halo, SiO<sub>2</sub>), 2.03 (α-Fe,  $d_{110}$ ) Å.

**Data for 14.** Heterogeneous red and white powder. PXRD:  $d = 38.6$  (MCM-41,  $d_{100}$ ), 22.3 (MCM-41,  $d_{110}$ ), 19.3 (MCM-41,  $d_{200}$ ) Å.

**Data for 15.** Gray powder. PXRD:  $d = 37.9$  (MCM-41,  $d_{100}$ ), 21.8 (MCM-41,  $d_{110}$ ), 18.9 (MCM-41,  $d_{200}$ ), 4 (br halo, SiO<sub>2</sub>), 2.07 (γ-Fe,  $d_{111}$ ), 2.03 (α-Fe,  $d_{110}$ ) Å.

**Fitting Magnetization Data to the Langevin Function.** When superparamagnetic particles are present in a system, the isothermal magnetization versus magnetic field data should obey the Langevin function,

$$\frac{M}{M^S} = \coth\left(\frac{\mu H}{kT}\right) - \frac{kT}{\mu H} \quad (1)$$

where  $M$  is the magnetization of the sample,  $M^S$  is the saturation magnetization,  $\mu$  is the average magnetic moment of the particles,  $H$  is the magnetic field,  $k$  is Boltzmann's constant, and  $T$  is the temperature.<sup>6</sup> When a distribution of particles with different magnetic moments is present, the magnetization may be represented as a sum of the individual Langevin functions.<sup>6</sup> For example, if a bimodal distribution is present, then the data sets may be fitted to the sum of two Langevin functions,

$$M = M_S^S \left[ \coth\left(\frac{\mu_S H}{kT}\right) - \frac{kT}{\mu_S H} \right] + M_L^S \left[ \coth\left(\frac{\mu_L H}{kT}\right) - \frac{kT}{\mu_L H} \right] \quad (2)$$

where  $M_S^S$ ,  $M_L^S$ ,  $\mu_S$ , and  $\mu_L$  distinguish the saturation magnetization and magnetic moment of the small and large particles, respectively.

As  $M$  vs  $H$  data for **9b–d** (300 K) fit very poorly to eq 1, they were fitted to eq 2. Initial estimates for  $M_S^S$ ,  $M_L^S$ ,  $\mu_S$ , and  $\mu_L$  were made by solving a system of four equations using representative data points. The variables were then refined by least squares to minimize  $\sum w_i (M_{\text{expt}} - M_{\text{calc}})^2$ , where the weighting factor  $w_i$  for the  $i$ th data point was equal to  $H_{i+1} - H_{i-1}$  (to compensate for the uneven density of data points collected as a function of magnetic field). The points at highest and lowest field were weighted with  $w_i$  equal to  $2(H_i - H_{i-1})$  and  $2(H_{i+1} - H_i)$ , respectively. The curves fit well to two Langevin equations as signified by low  $\chi^2$  values and correlation coefficients ( $R^2$ ) close to 1. Each of the two components was resolved from the function and best-fit values of  $M_S^S$ ,  $M_L^S$ ,  $\mu_S$ , and  $\mu_L$  are listed in Table 2.

If the particles are assumed to be spherical, to have the same density as the bulk phase, and to possess the same saturation magnetization as

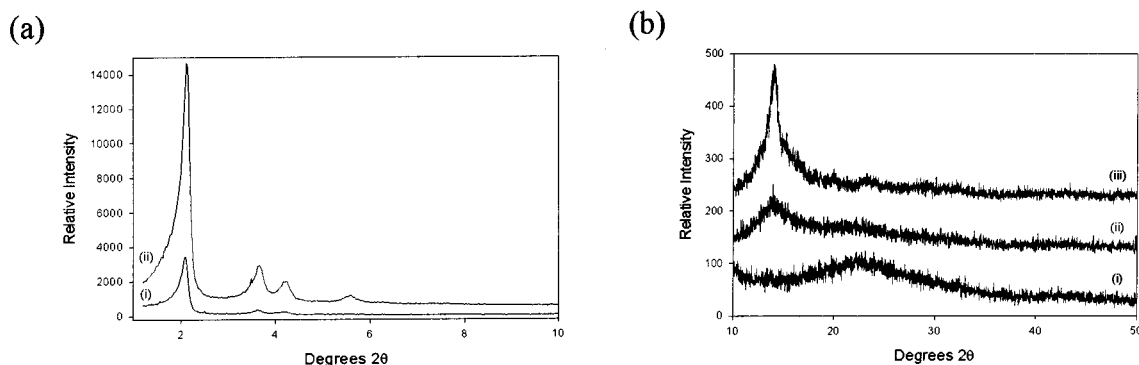


**Figure 1.** (a) Low-angle PXRD patterns of (i) **5c** and (ii) calcined ODA-MCM illustrating the decreased intensity observed in the hexagonal reflections after introducing **1** into the mesoporous silica host. (b) High-angle PXRD patterns of (i) calcined ODA-MCM, (ii) **5c**, and (iii) amorphous polymer **2**.

the bulk phase ( $M_B^S$ ), then the average magnetic particle diameter,  $D_{\text{mag}}$ , can be calculated from the magnetic moment  $\mu$  as follows:<sup>26</sup>

$$D_{\text{mag}} = \left( \frac{6\mu}{\pi M_B^S} \right)^{1/3} \quad (3)$$

For the calculations reported in this paper, the saturation magnetization values of Fe and  $\text{Fe}_3\text{O}_4$  were assumed to be 1700 and 480 emu  $\text{g}^{-1}$ , respectively.

The histogram of particle-size distribution was obtained by measuring about 150 particles in a TEM image. The standard deviation,  $\sigma$ , was calculated as the square root of the variance using the equation

$$\sigma = \sqrt{\frac{1}{N} \sum_i (N_i(D_i - D)^2)}$$

where  $D$  and  $N$  are the average diameter and number of particles, respectively. A single particle that was about twice the size of any other particle in the image was neglected. Moreover, particles smaller than ca. 2 nm in the image (2 nm) were not included as they could not be easily distinguished from the sample roughness and granularity of the image.

## Results and Discussion

**Synthesis and Characterization of  $\text{fcSiMe}_2/\text{MCM-41}$  Composites **5**.** Ferrocenophane **1** was introduced into MCM-41 by vapor deposition. Thus, dehydrated MCM-41 was combined with monomer **1** in a Schlenk tube under vacuum to allow the monomer to sublime into the channels. Initially, the heterogeneous mixture contained white powder and red crystals but changed to a homogeneous orange powder over several days. The partially and fully loaded products obtained after subliming excess monomer **1** at room temperature were investigated by multiple techniques.

From the synthesis of several samples, the maximum loading occurred when a weight ratio of 74% ( $\pm 5\%$ ) of **1** to host MCM-41 was used. Fe analysis of a representative sample that was completely loaded with **1** inside ODA-MCM (**5c**) indicated that it contained 5.4 wt % Fe, corresponding to an organometallic content of 24 wt % (31 mg of **1** per 100 mg of host). This is substantially less than the loading reported by O'Brien et al. where the composite contained approximately 40 wt % of organometallic species.<sup>23</sup> Fe analysis of a sample prepared starting with ca. 33 mg of guest per 100 mg of hydrated host (**5a**) indicated that it contained 3.45 wt % Fe, corresponding to an organometallic content of 15 wt % (ca. 18 mg of guest **1** per 100 mg of host).

PXRD confirmed that none of the samples **5a–d** contained excess crystalline monomer. Moreover, the positions of the reflections assigned to calcined MCM-41 were essentially unchanged, indicating that the long-range hexagonal order of the mesoporous host was maintained. Samples prepared with mesoporous silica templated by both ODA-MCM and cetylpyridinium chloride (CPM-MCM) displayed a large decrease in peak intensity upon filling the material with monomer **1** (Figure 1a). This phenomenon results from a reduction in the electron contrast between the channel walls and interior and is consistent with loading of the channels in the mesoporous material.<sup>27</sup> Moreover, in the region of  $2\theta = 12\text{--}16^\circ$ , a new amorphous halo emerged that is characteristic of amorphous poly(ferrocenylsilanes) (Figure 1b). MCM-41 possesses a broad halo at  $2\theta = 15\text{--}30^\circ$ , characteristic of amorphous silica channel walls.

IR spectroscopy of the samples showed absorptions expected for vibrations of ferrocenylsilane moieties<sup>16</sup> and the silica framework. Upon further loading, the intensity of the peaks attributed to C–H stretching increased relative to the Si–O stretching peak ( $1083\text{ cm}^{-1}$ ). Furthermore, the broad O–H stretching peak near  $3400\text{ cm}^{-1}$  was noticeably more intense in the partially loaded sample **5a** compared with the fully loaded sample **5c**, as expected if fewer of the SiOH groups were reacted in the partially loaded sample **5a**. This confirmed the titration of silanol OH groups with ferrocenophane **1** as the channels were filled with the organometallic species.

Reflectance UV–vis spectra of the orange-yellow solids **5a–d** were all similar, showing intense bands characteristic of ferrocene moieties. Notably, a broad absorption at 458 nm corresponding to a d–d transition characteristic of the ferrocenyl groups is blue shifted relative to monomer **1** ( $\lambda_{\text{max}} = 487\text{ nm}$  in  $\text{CH}_2\text{Cl}_2$ ). This hypsochromic shift is typical of ring-opening [1]ferrocenophanes.<sup>28</sup> The presence of a weak absorption at 627 nm in **5a** signaled the presence of trace ferrocenium moieties, possibly generated from protonation of Fe(II) from acidic silanol groups within the sample. Reflectance near-IR spectroscopy of **5a–d** showed resonances at ca. 1660–1760 nm corresponding to overtones of the stretching frequencies for the ferrocenyl moieties.

The loading of **1** into MCM-41 was monitored by solid-state NMR spectroscopy. Figure 2a shows the  $^1\text{H}$  magic-angle spinning (MAS) NMR spectra of the composites **5a–c** as **1** was loaded into the channels of ODA-MCM. The partially loaded

(27) Marler, B.; Oberhagemann, U.; Vortmann, S.; Gies, H. *Microporous Mater.* **1996**, 6, 375.

(28) (a) Osborne, A. G.; Whiteley, R. H.; Meads, R. E. *J. Organomet. Chem.* **1980**, 193, 345. (b) Rulkens, R.; Gates, D. P.; Balaishis, D.; Pudelski, J. K.; McIntosh, D. F.; Lough, A. J.; Manners, I. *J. Am. Chem. Soc.* **1997**, 119, 10976.

(26) Charles, S. W.; Popplewell, J. In *Ferromagnetic Materials*; Wohlfarth, E. P., Ed.; North-Holland Publishing: Amsterdam, 1982; Vol. 2.

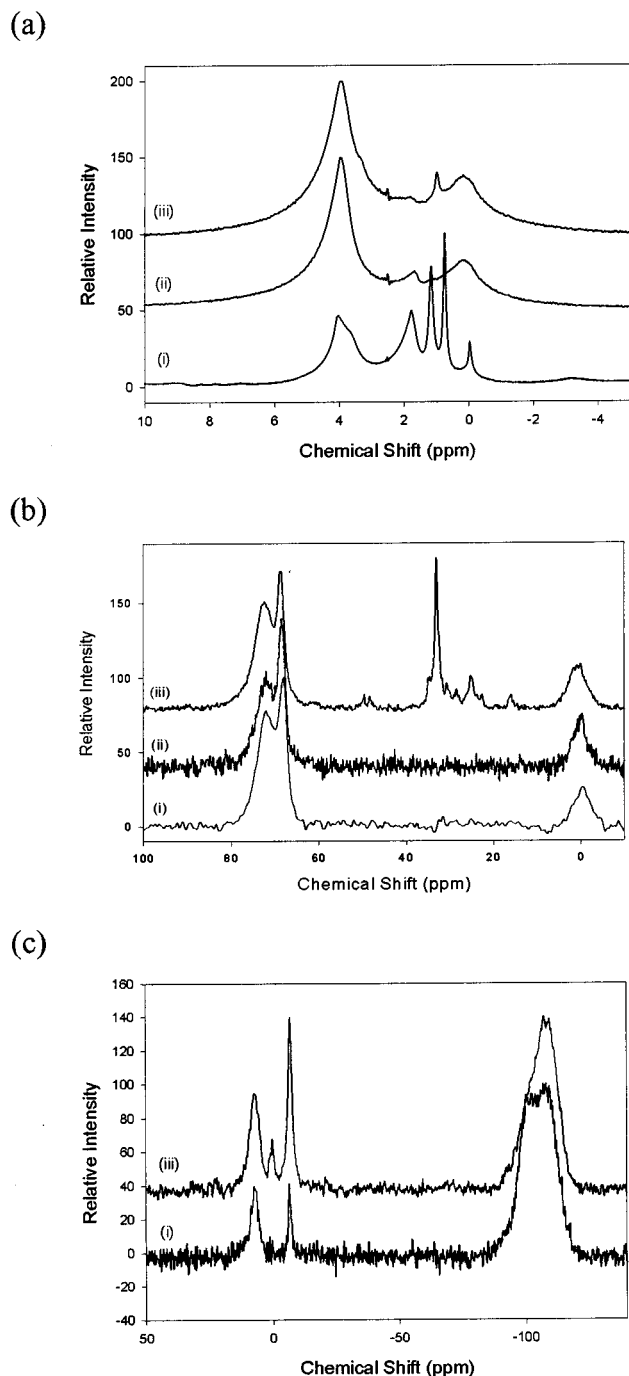
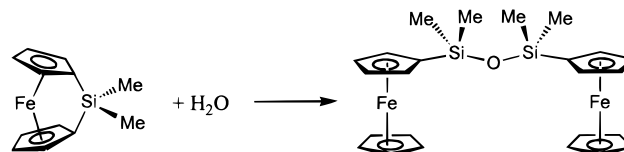


**Figure 2.** (a)  $^1\text{H}$  MAS NMR spectra, (b)  $^{13}\text{C}$  CP-MAS NMR spectra, and (c)  $^{29}\text{Si}$  CP-MAS NMR spectra of (i) **5a**, (ii) **5b**, and (iii) **5c**.

composite, **5a**, shows several peaks that are attributed to protons of ferrocenyl, methyl, and OH groups in the channels of MCM-41. Upon full loading with **1**, nearly all of the OH sites have reacted with monomer to form ring-opened species, and new peaks attributed to  $\text{CH}_3$  groups of the ferrocenylsilanes are observed. The  $^{13}\text{C}$  cross-polarization (CP) MAS NMR spectra of the same series are shown in Figure 2b. A partially loaded sample (**5a**) of MCM-41 showed resonances consistent with ring-opened species, showing only a broad methyl resonance near 0 ppm, a free Cp resonance at 68.0 ppm, and other Cp resonances near 72 ppm. When the MCM-41 was loaded with excess monomer, several new resonances emerged between 16 and 50 ppm that are attributed to the *ipso*-C of the Cp ligands in **1**, present in different chemical environments in the composite.

$^{29}\text{Si}$  CP-MAS NMR spectra of each of the samples examined showed resonances at  $-100$  to  $-120$  ppm, near 7 ppm, and near  $-7$  ppm.  $^{29}\text{Si}$  NMR spectra of composites **5a** and **5c** are shown in Figure 2c.  $\text{Q}_3$  ( $\text{SiO}_3(\text{OH})$ ) and  $\text{Q}_4$  ( $\text{SiO}_4$ ) resonances of silica are observed at  $-100$  to  $-120$  ppm. Upon loading the channels with monomer **1**, there was a noticeable decrease in the intensity of resonances assigned to  $\text{Q}_3$  silicon atoms (ca.  $-100$  ppm). This would be expected if monomer **1** reacted with the silanol groups on the surface. Although the use of CP limits the quantification of these Si assignments, the same observation has been made by others.<sup>23</sup> The chemical shift of 7 ppm is assigned to  $\text{CpSiMe}_2\text{O}$  environments by comparison with similar species in the literature.<sup>29</sup> These sites are attributed either to ferrocenophane **1** attached to the silica via ring-opening addition of a silanol group to the Si–Cp bond, or to oligomers attached to the surface of the silica via an Si–O–Si linkage. The narrow resonance at ca.  $-7$  ppm is assigned to oligomers and polymer **2**,  $[\text{FcSiMe}_2]_n$  (cf.  $^{29}\text{Si}$  NMR of  $[\text{FcSiMe}_2]_n$ :  $\delta = -6.4$  ppm in  $\text{C}_6\text{D}_6$ ).<sup>13</sup> Samples **5c** and **5d** also showed a smaller resonance near 0 ppm, a signal that was not observed in the partially loaded sample **5a**. We speculate that this arises from  $(\text{FcSiMe}_2)_2\text{O}$  trapped inside the channels ( $^{29}\text{Si}$  NMR of  $(\text{FcSiMe}_2)_2\text{O}$ :  $\delta = 0.4$  ppm).<sup>30</sup> This compound may form in the presence of any water in the silica (Scheme 2) and would be retained in the

#### Scheme 2



pores. Ferrocenophane **1** would be expected to react much faster with acidic silanol groups inside the channel than with water, explaining why the partially loaded sample, which still contained a substantial number of silanol groups, did not show this disiloxane species. In addition, O'Brien et al. did not observe the disiloxane by solid-state NMR as it would have been washed from their sample in the solution phase preparation.<sup>23</sup>

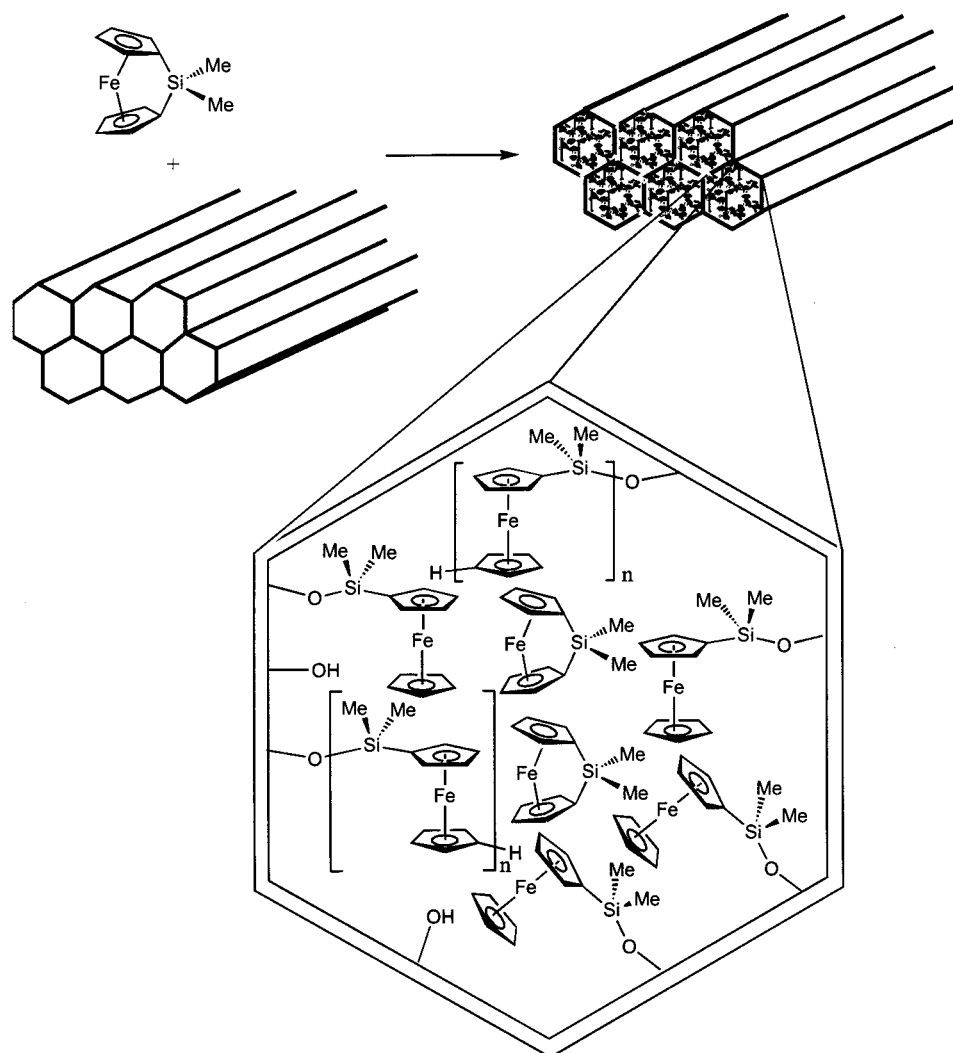
Our evidence suggests that ring-opened and oligomeric products, bound to the  $\text{SiO}_2$ , are present inside the channels of MCM-41 (Scheme 3). This is consistent with the NMR and EXAFS results of O'Brien et al.<sup>23</sup> We believe that our results also show that the ferrocenylsilanes are *inside* the channels of MCM-41. Although there is undoubtedly a monolayer on the exterior surface, bound by surface hydroxyl groups, the surface area inside MCM-41 is much greater than on the outside. The dramatic intensity reduction observed in the PXRD patterns upon loading the channels cannot be accounted for by a physical mixture of the monomer and MCM-41. Moreover, the absence of crystalline species in the PXRD pattern is consistent with the inclusion of the ferrocenylsilanes. At very high loading, free monomer could be trapped inside the channels. We investigated the polymerization of free **1** within the channels of MCM-41.

**Polymerization of 1 in MCM-41.** When **1** was studied by DSC, the ferrocenophane melted near  $75^\circ\text{C}$  and then underwent exothermic ROP. Composites partially loaded with **1** (samples **5a** and **5b**) showed neither the melt transition nor the ROP exotherm when examined by DSC. However, DSC analysis of **5c** revealed a broad exotherm corresponding to ROP of **1** between  $75$  and  $200^\circ\text{C}$ . The absence of an endothermic melt

(29) Sindorf, D. W.; Maciel, G. E. *J. Am. Chem. Soc.* **1983**, *105*, 3767.

(30) Angelakos, C.; Zamble, D. B.; Foucher, D. A.; Lough, A. J.; Manners, I. *Inorg. Chem.* **1994**, *33*, 1709.

Scheme 3



transition for **5c** indicates that the free monomer was not crystalline, in contrast to bulk **1**. This is consistent with the absence of high-angle diffraction peaks in the PXRD of **5c**. It is unlikely that monomer trapped within the narrow channels of MCM-41, where ring-opened monomeric and oligomeric species are tethered to the walls, would be able to crystallize. The breadth of the ROP exotherm may result from the inhomogeneity of the trapping sites of **1** inside MCM-41. Monomer molecules may be near oligomers, polymers, or silica inside the channels, and their orientations may vary. Integration of the curve from DSC scans of **5c** indicated an enthalpy change of  $6(2) \text{ J g}^{-1}$ . Given that the enthalpy of polymerization of **1** is ca.  $-330 \text{ J g}^{-1}$ <sup>13,31</sup> and that **5c** contained ca. 31 mg of **1** per 100 mg of host (from Fe analysis), sample **5c** contained approximately 2 wt % of free monomer **1** (i.e., ca. 8% of monomer **1** introduced into the channels of MCM-41 was present as free monomer). It is noteworthy that the partially loaded samples, **5a** and **5b**, did not show an exotherm in the DSC, as expected if they did not contain excess monomer.

To examine the bulk polymerization, a sample of **5c** was heated at  $140^\circ\text{C}$  under  $\text{N}_2$  for 4 h to give a yellow solid, **6**.  $^1\text{H}$  NMR,  $^{29}\text{Si}$  NMR, and PXRD of the polymerized sample were essentially identical to those for sample **5c**. Moreover, the reflectance UV-vis/near-IR spectrum of **6** was nearly the same as that of **5c**, with the d-d transition observed at 457 nm. However, the  $^{13}\text{C}$  CP-MAS NMR spectrum of the polymerized

sample showed no ferrocenophane *ipso*-C atoms present using the same NMR acquisition parameters as for **5c**. These results are consistent with the ROP of a very small amount of excess **1** within the channels of MCM-41.

**Synthesis and Characterization of  $\text{FeSi}(\text{CH}_2)_3/\text{MCM-41}$  Composite 7.** We have recently shown that ceramic yields from poly(ferrocenylsilanes) are drastically improved when the polymer is cross-linked.<sup>17b,c</sup> Incorporation of monomer **3**, which possesses two strained rings, into MCM-41 should give an improved ceramic precursor if it undergoes cross-linking, perhaps facilitating the synthesis of extractable ceramic nanofibers in the channels. Composite **7** was prepared by vapor deposition using a procedure similar to that used to incorporate **1** into MCM-41, though it was necessary to sublime at ca.  $45^\circ\text{C}$  to remove all excess monomer from the product. Fe analysis of a representative sample indicated that the sample contained 4.3 wt % Fe, corresponding to an organometallic content of 20 wt % (i.e., 24 mg of **3** per 100 mg of host).

PXRD confirmed that the long-range order of the hexagonal mesoporous material was maintained. Like **5a-d**, composite **7** showed decreased PXRD intensities compared to calcined MCM-41, consistent with impregnation of the monomer into the channels. A broad halo observed at  $2\theta = 10-20^\circ$  is characteristic of amorphous poly(ferrocenylsilanes).

Figure 3 shows the results of solid-state NMR studies of **7**. The  $^1\text{H}$  MAS NMR spectrum of **7** showed a single broad



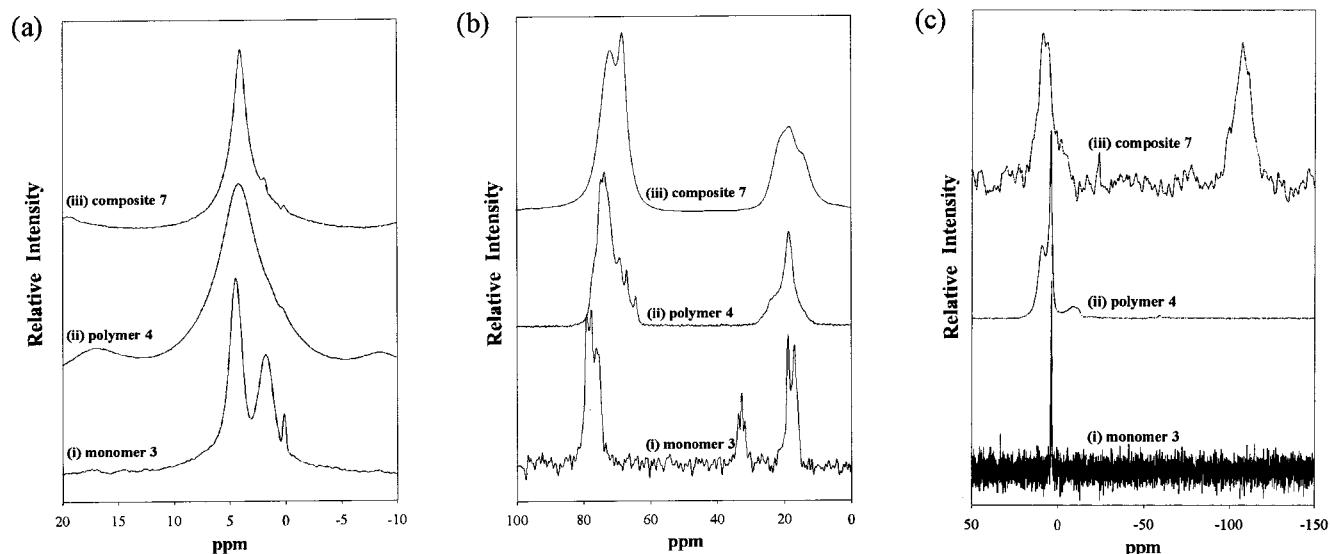


**Figure 3.** (a)  $^1\text{H}$  MAS NMR spectra, (b)  $^{13}\text{C}$  CP-MAS NMR spectra, and (c)  $^{29}\text{Si}$  CP-MAS NMR (i) spectra of monomer **3**, (ii) polymer **4**, and (iii) composite **7**.

resonance near 4 ppm. It is noteworthy that the peak is substantially narrower than the same peak observed in polymerized **3**, indicative of enhanced mobility. In the  $^{13}\text{C}$  NMR spectrum of **7**, broad peaks centered at 17.8 and 14.6 ppm are assigned to the silacyclobutane group. Peaks at 68.3 and 72.2 ppm are assigned to free Cp and SiCp resonances, respectively.  $^{29}\text{Si}$  NMR of **7** showed broad resonances at 8.8 and  $-107$  ppm, assigned to Si from ring-opened **7** and MCM-41, respectively. The NMR results are consistent with monomer that has been ring-opened by the silanol groups to afford ring-opened monomeric and oligomeric species within the mesoporous host. For comparison, the  $^{29}\text{Si}$  NMR resonance for  $[\text{FcSi}(\text{CH}_2)_3]_2\text{O}$  is observed at 0.54 ppm in  $\text{C}_6\text{D}_6$ .<sup>32</sup>

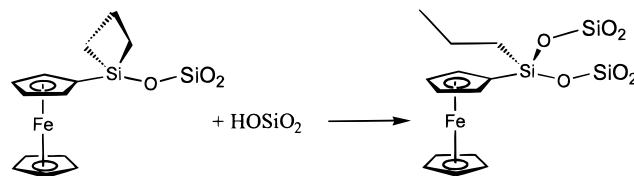
The UV–vis absorption of the ferrocenyl groups in composite **7** (453 nm) was blue-shifted by 25 nm compared with monomer **3**, consistent with ring-opening of the [1]ferrocenophane.<sup>28</sup> For comparison,  $[\text{FcSi}(\text{CH}_2)_3]_2\text{O}$ , which structurally resembles ring-opened monomer **3** attached to silica, has  $\lambda_{\text{max}} = 451$  nm in  $\text{CH}_2\text{Cl}_2$ .<sup>32</sup> A charge-transfer band observed at 299 nm in monomer **3** was observed at 270 nm in composite **7**, consistent with a substantial structural change in the ferrocenyl moiety upon incorporation into MCM-41.

IR spectroscopy of **7** was consistent with the presence of ferrocenylsilane moieties inside MCM-41. Modes attributed to  $\nu\text{C-H}$  stretching were observed at  $3097\text{ cm}^{-1}$  for the Cp ligands and  $2967$ ,  $2929$ , and  $2874\text{ cm}^{-1}$  for the methylene groups. The high frequency of the first aliphatic C–H stretch is characteristic of a closed silacyclobutane ring in which the symmetric  $\nu\text{C-H}$  stretching frequency is elevated due to the ring strain.<sup>33</sup> For comparison, monomer **3** shows aliphatic  $\nu\text{C-H}$  stretching modes at  $2970$ ,  $2943$ ,  $2924$ , and  $2867\text{ cm}^{-1}$ .

These results are consistent with the presence of ring-opened monomer **3** and oligomers tethered to the walls of the mesoporous host with the silacyclobutane rings intact. To clarify whether the silacyclobutane rings were still closed, polymerization of composite **7** was undertaken.

**Polymerization of 3 in MCM-41.** Our studies of  $[\text{FcSi}(\text{CH}_2)_3]_2\text{O}$  have indicated that this monomer undergoes thermal ROP of the silacyclobutane rings at  $240\text{ }^\circ\text{C}$ .<sup>32</sup> To test if the silacyclobutane rings in composite **7** would undergo ROP, a sample of **7** was heated under  $\text{N}_2$  at  $280\text{ }^\circ\text{C}$  for 4 h. The  $^{13}\text{C}$  CP-MAS NMR spectrum of the resulting material **8** was similar to that of composite **7**, but the  $^{29}\text{Si}$  CP-MAS NMR spectrum of **8** was substantially changed from that of **7**, showing broad peaks at ca.  $-107$ ,  $-58$ ,  $-25$ ,  $5$ , and  $9$  ppm assigned to  $\text{SiO}_2$  (host),  $[\text{RSiO}_3]$  (host),  $[\text{R}_2\text{SiO}_2]$  (guest),  $[\text{R}_3\text{SiO}]$  (guest), and  $[\text{R}_3\text{Si}]$  (guest), respectively. These new peaks are consistent with ring-opening of silacyclobutane within the channels. The small amount of  $\text{RSiO}_3$  observed likely arises from  $-\text{CH}_2\text{SiO}_3$  groups, where a reactive silacyclobutane has reacted with a silicon of the host. All of the peaks in the NMR spectrum are broad, indicating that the species are immobile as expected for cross-linked polymers and monomers pinned to the channels. IR spectroscopy of **8** indicated small structural changes to the ferrocenylsilane encapsulated in the MCM-41. In the aliphatic C–H stretching region, peaks were observed at  $2962$  ( $\nu_{\text{as}}\text{CH}_3$ ),  $2932$  ( $\nu_{\text{as}}\text{CH}_2$ ), and  $2876\text{ cm}^{-1}$  ( $\nu_{\text{s}}\text{CH}_2$  and  $\text{CH}_3$ ). Moreover, a reduction in intensity of the O–H stretching frequency (ca.  $3450\text{ cm}^{-1}$ , broad) was observed in **8** relative to **7**. These results suggest that the silacyclobutane rings in **7** opened after thermal treatment, but reacted at least partially by ring-opening addition of O–H to the Si– $\text{CH}_2$  bond, forming a propyl group on silicon (Scheme 4). This may be accompanied by ROP of the

#### Scheme 4



silacyclobutanes, but polymeric carbosilane could not be distinguished from the silacyclobutane groups ring-opened with terminal silanol groups present in the MCM-41.

**Pyrolysis Study of 5a–d and 7.** We have previously reported the pyrolysis of poly(ferrocenylsilanes) to afford ceramics containing Fe particles inside a Si/C/N matrix.<sup>15,17c</sup> By pyrolyzing composites **5**, we hoped to form Fe nanostructures

(31) Foucher, D. A. *Synthesis and Properties of New Silicon Containing Inorganic and Organometallic Polymers*. Ph.D. Thesis, University of Toronto, 1993.

(32) MacLachlan, M. J.; Thieme, K.; Ginzburg, M.; Lough, A. J.; Manners, I. Manuscript in preparation.

(33) Silverstein, R. M.; Bassler, G. C.; Morrill, T. C. *Spectrometric Identification of Organic Compounds*, 5th ed.; John Wiley & Sons: Toronto, 1991; p 105.

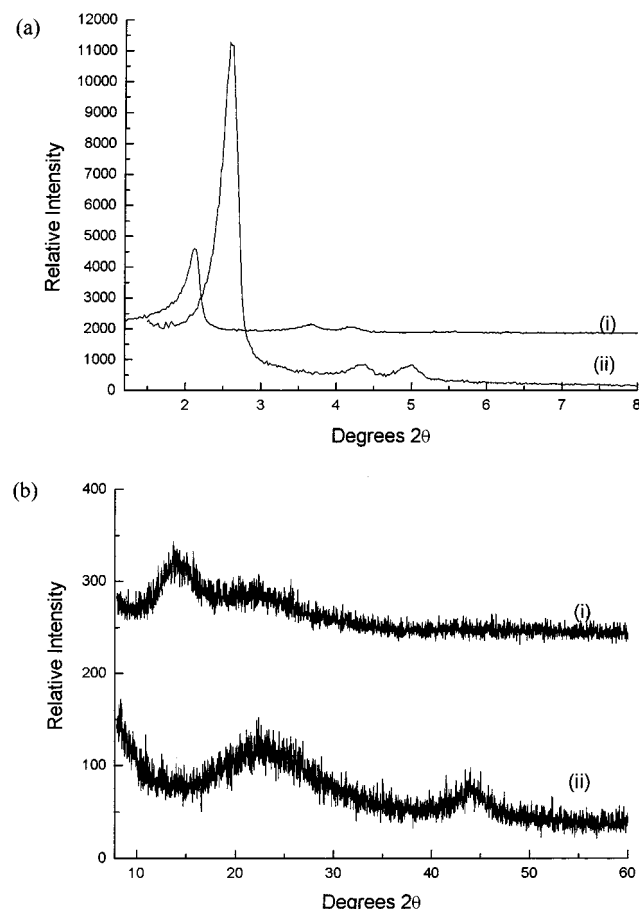


**Figure 4.** PXRD patterns of an MCM-41/1 composite (i) before and (ii) after pyrolysis showing the (a) low-angle and (b) high-angle transformations that occur.

confined to the channels of MCM-41. Samples of **5a–d** were heated at 900 °C for 2 h under a slow flow of N<sub>2</sub> to yield ceramics **9a–d**. The yellow powder was transformed into a fine black powder that was attracted to a magnet. A small amount of ferrocene sublimed from the material during the pyrolysis and collected on the cold part of the pyrolysis tube. Ceramic yields of 69–86% were obtained. As expected, the highest yields were for the lowest loadings of **1** in MCM-41 since calcined MCM-41 alone shows little mass loss up to 900 °C.

Figure 4 shows the PXRD patterns of a typical composite before and after pyrolysis. At low angles, PXRD revealed a contracted interpore distance resulting from the condensation polymerization of residual SiOH groups in the silica channels after pyrolysis. An enhanced peak intensity relative to the loaded sample is consistent with a structural improvement of the channel walls and the loss of considerable electron density from within the channels as the polymer was transformed into a ceramic. At higher angles, the amorphous halo attributed to the ferrocenylsilane polymer ( $2\theta = 14^\circ$ ,  $d = 6.3$  Å) had disappeared from the ceramic and a new peak near  $2\theta = 45^\circ$  ( $d = 2.03$  Å) had emerged. This latter peak is assigned to the (110) reflection of  $\alpha$ -Fe. As a consequence of the very small  $\alpha$ -Fe particle sizes in the samples, the peak is substantially broader (e.g., full width at half-maximum (fwhm) for **9b** was  $\Delta\theta = 6.2(4)^\circ$ ) than for bulk  $\alpha$ -Fe (fwhm:  $\Delta\theta = \sim 0.18^\circ$ ). The Scherrer equation (eq 4) was employed to calculate the particle size of the Fe nanocrystallites.<sup>34</sup>

$$L_{hkl} = [0.9\lambda/B \cos \theta] \quad (4)$$

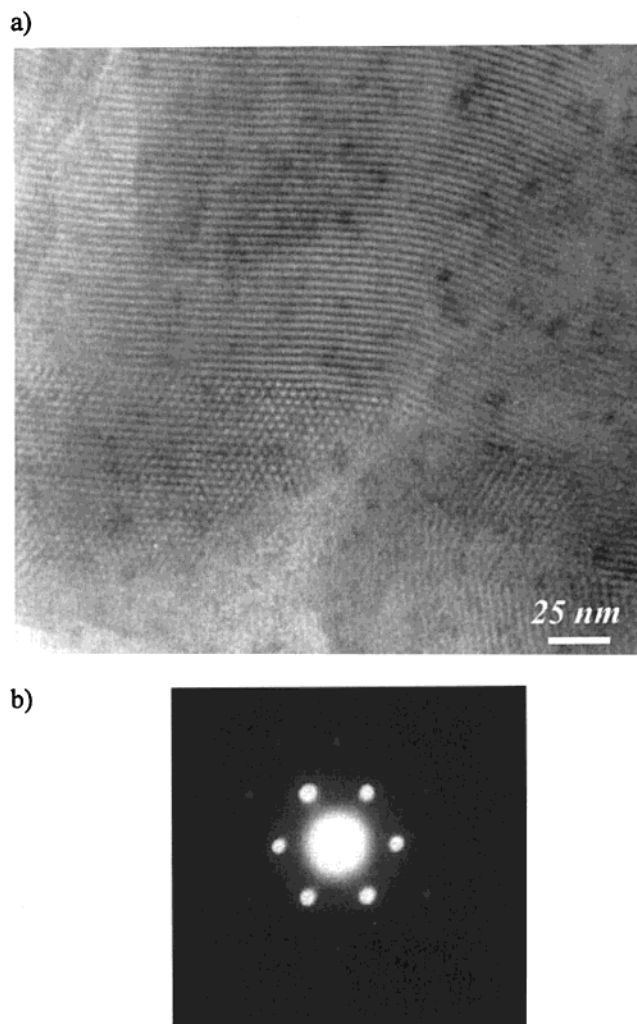


**Figure 5.** (a) TEM image of ceramic **9d**. The striped region shows the MCM-41 mesostructure parallel to the channel axis, while the remainder illustrates the hexagonal mesostructure perpendicular to the channel axis. (b) Electron diffraction of **9c** reflecting the hexagonal order in the ceramic.

where  $L_{hkl}$  is the average diameter of the crystallites,  $B = [B^2_{\text{measured}} - B^2_{\text{standard}}]^{1/2}$  is the root-mean-square difference between the angular fwhm for the sample with respect to a powder Fe standard (radians),  $\lambda$  is the wavelength of the X-ray radiation, and  $\theta$  is the Bragg angle for the reflection (radians). Fe<sub>3</sub>O<sub>4</sub> or Fe<sub>2</sub>O<sub>3</sub> and Fe were evident in **9a**, but only Fe was evident by PXRD in **9b–d**. It was assumed that the Fe nanoparticles were only  $\alpha$ -Fe, though the peaks were broad enough to conceal the (111) reflection of any  $\gamma$ -Fe present. Peaks were fitted several times with standard peak-fitting software to give an estimate of the error in the fwhm. Using the Scherrer equation, we calculated particle sizes of 28(2), 31(2), and 41–(5) Å for samples **9b**, **9c**, and **9d**, respectively. The iron nanoparticles in **9b** and **9c** are virtually identical in size and appear to be confined to the channels of the mesoporous host. The iron nanoparticles in **9d**, however, appear larger and may have grown out of a single channel.

It is worth noting how the pyrolysis of the poly(ferrocenylsilane) within the ordered channels of mesoporous silica differs from the bulk pyrolysis of **2**. The Fe nanoparticles obtained in MCM-41 are substantially smaller than the particles obtained

(34) Guinier, A. *X-Ray Diffraction in Crystals, Imperfect Crystals, and Amorphous Bodies*; Dover: New York, 1994; p 124.

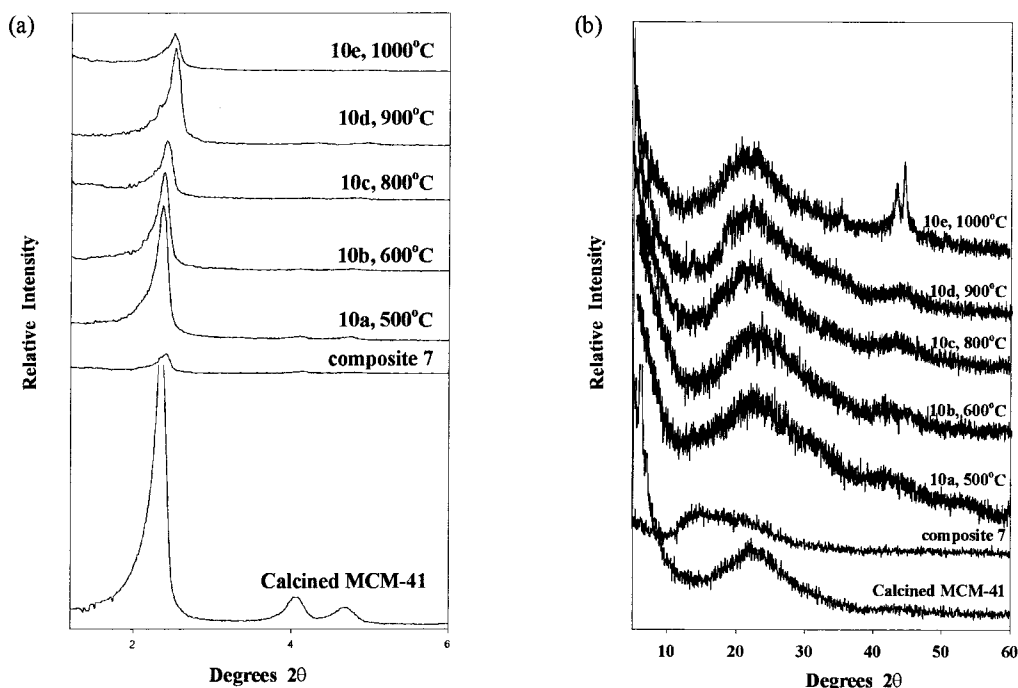


**Figure 6.** PXRD patterns for calcined CPM-MCM, composite 7, and ceramics **10a–e** at (a) low angles and (b) high angles. (Note that **10d** was prepared using a different sample of composite 7 from the others.)

from the bulk pyrolysis. Additionally, neither graphite nor  $\alpha$ - $\text{Si}_3\text{N}_4$  was observed in the pyrolyses, compositions that were obtained from the bulk pyrolysis of **2**.<sup>15,17c</sup>

The samples were imaged by transmission electron microscopy (TEM). Figure 5a shows a TEM image of ceramic **9d**. Fe nanoparticles are confined to the channels, though some “appear” to be larger than a single channel. A particle-size distribution could not be determined from the TEM images due to the difficulty of distinguishing the edges of particles from the silica walls. The mesostructured order of the MCM-41 host material was evidently maintained at even 900 °C. The walls appeared slightly thicker and showed greater electron contrast than MCM-41 itself. This is consistent with the structural improvement and contraction of the hexagonal unit cell of the host. An electron diffraction (ED) pattern of the ceramic composite **9c** is shown in Figure 5b. The observation of ED up to the third order (300) indicates the excellent structural order of the hexagonal mesostructure. The  $d_{100}$  spacing obtained from the ED pattern (the  $d_{100} \approx 45$  Å) is similar to the value obtained from PXRD ( $d_{100} \approx 42$  Å).

Samples of **7** were pyrolyzed under nitrogen for various times to examine the changes that occur to the ceramic; conditions are summarized in Table 1. After pyrolysis, powders (**10**) were obtained in 73–85% yields.

The pyrolysis of **7** was monitored by PXRD. Figure 6 shows the PXRD patterns of ceramics **10a–e**. Although the silica underwent further polymerization-induced contraction during heating, the hexagonal mesoporous structure of the host was maintained up to 1000 °C. PXRD indicated that the ferrocenylsilane guest had already undergone a large structural transformation by 500 °C as the broad amorphous halo at  $d = 6.3$  Å, a signature of ferrocenylsilanes, had disappeared, leaving only the amorphous halo at  $d = 4$  Å, characteristic of  $\text{SiO}_2$ . A peak that has been assigned to the  $d_{110}$  of  $\alpha$ -Fe first emerged at 600 °C and grew to 900 °C. In the PXRD pattern of the sample prepared at 1000 °C (**10e**), peaks assigned to both the high-temperature  $\gamma$ -Fe (fcc) and low-temperature  $\alpha$ -Fe (bcc) were apparent, as well as a peak due to magnetite,  $\text{Fe}_3\text{O}_4$ .

Figure 7 shows TEM images of **10b** and **10e** (microtomed). The ceramic prepared at 600 °C (**10b**) shows very small Fe nanoparticles that appear confined to single channels. In the sample prepared at 1000 °C, however, the particles are much larger and nearly round. The particles visible in the TEM image were counted and are plotted in a histogram in Figure 7c. The particle-size distribution is monomodal, and the average particle size was calculated to be  $10.8 \pm 3.9$  nm (histogram in Figure 7c). Using the Scherrer equation, the size of the Fe particles were ca. 20–40 nm in diameter. This clearly overestimates the size observed in the TEM micrograph. There may be larger particles, which were not observed by TEM, that contribute significantly to the particle size determined by PXRD. The  $\text{Fe}_3\text{O}_4$  observed in the PXRD pattern may exist as a surface coating on the Fe particles.

Samples were pyrolyzed at 1000 °C for different lengths of time and examined by PXRD (Figure 8). After 6 h at 1000 °C, the mesoporous structure was still present in the sample (**10f**), although the intensity of the peaks was reduced relative to the sample prepared for 1 h (**10g**). Both  $\alpha$ -Fe and  $\gamma$ -Fe as well as  $\text{Fe}_3\text{O}_4$  were present in this sample. After 24 h of pyrolysis at 1000 °C (**10h**), however, an enormous change had occurred to the composite structure. No evidence for mesoporosity was apparent in the PXRD pattern of the material, **10h**. Moreover, the halo at  $d = 4$  Å, attributed to glassy  $\text{SiO}_2$ , was less intense, giving way to crystalline quartz and cristobalite in the sample. Both forms of Fe as well as magnetite were still present in the sample. This is, to our knowledge, the first observation of the transformation of mesoporous silica to quartz.

Finally, a sample of **7** was pyrolyzed under the same conditions as used to prepare sample **9d**. Although the ceramic yield was slightly higher for **10i** than for **9d**, there appears to be no substantial difference between products prepared when monomer **1** or **3** was inside the mesoporous silica. Ceramic **10i** showed a broad halo near 2.1 Å, consistent with  $\alpha$ -Fe, and some  $\text{Fe}_3\text{O}_4$ .

**Control Pyrolysis Studies.** To confirm that our chemistry takes place *inside* the channels of MCM-41, several control experiments were performed. A composite prepared under



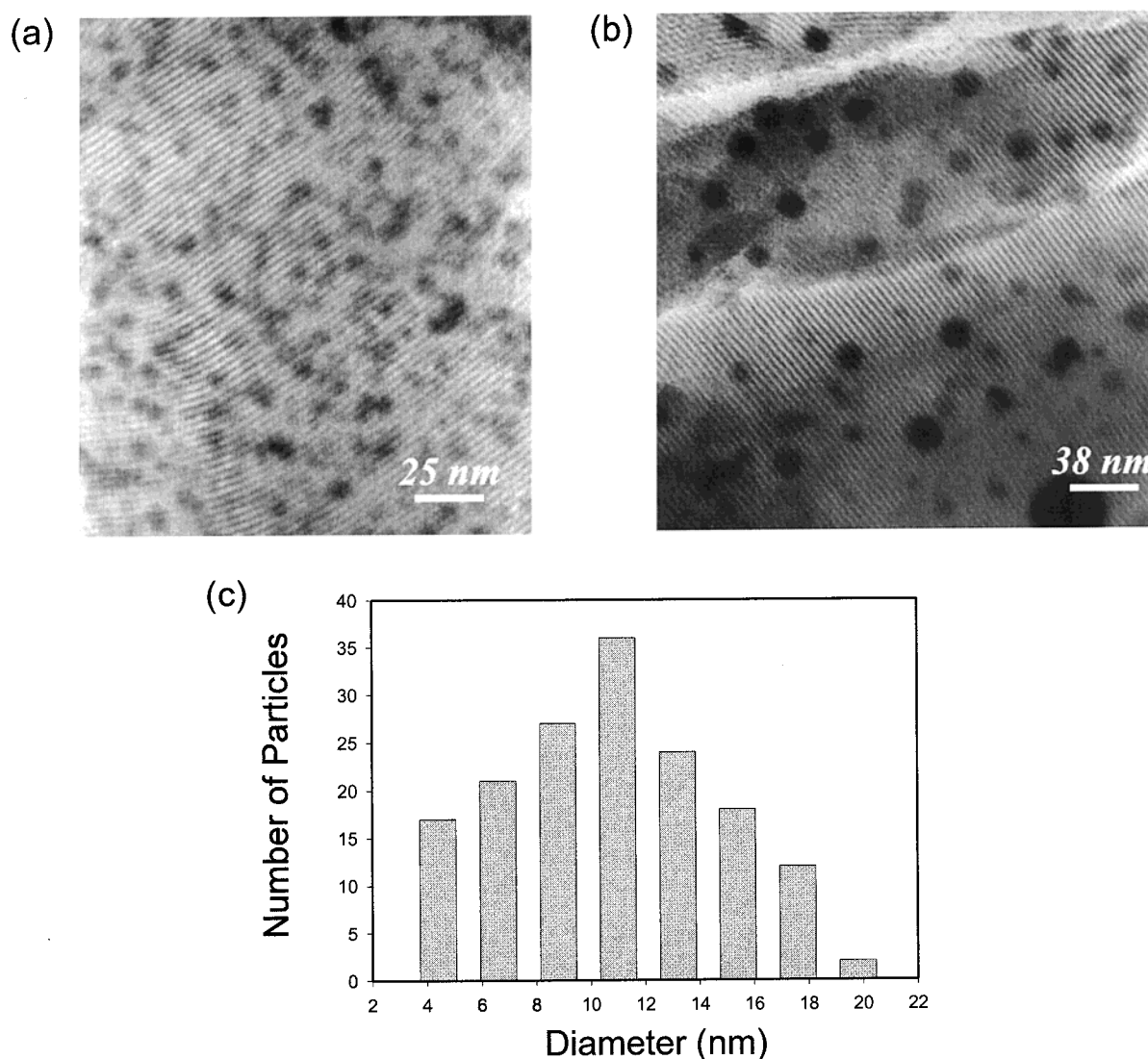


**Figure 7.** TEM images of (a) ceramic **10b** prepared at 600 °C and (b) ceramic **10e** prepared at 1000 °C which show Fe nanoparticles in the ordered channels of MCM-41. (c) A histogram of the particle-size distribution as measured from a TEM image of ceramic **10e**.

similar conditions to those used to prepare **5a–d** with amorphous silica in the place of MCM-41 was pyrolyzed at 900 °C to yield **11**. Since excess monomer was sublimed off prior to pyrolysis, it is expected that only a monolayer of monomer would adhere to the surface. Fe nanoparticles were not apparent by PXRD, and only isolated Fe particles were observed by TEM. This further confirms that any iron present on the outside surface is not significant.

Further control samples **12** and **14** were prepared through physical mixing of MCM-41 and polymers **2** and **4**, respectively. The resulting composites were heterogeneous orange and white mixtures ( $\text{SiO}_2$ :polymer ratio was set to correspond with the elemental analyses determined for **5c** and **7**). When imbibed with monomer, the intensity of the 100 diffraction peak of the MCM-41 decreased by ca. 80–90% (e.g., 80% for **5a**, 90% for **5d**, 93% for **7**). However, the physical mixtures of monomer and MCM-41 showed significantly smaller intensity decreases for the 100 diffraction peak which correlated with the percent dilution of the mesoporous silica. This difference can be explained by the incorporation of monomer *inside* the mesoporous host for composites **5** and **7**, where the intensity reduction has two components: reduction due to dilution of the diffracting species; and reduction due to decrease of the electron contrast between the channels and the host walls.

Moreover, the MCM-41 diffraction peak intensity for samples with imbibed monomer/polymer (**5**, **7**) increased dramatically after pyrolysis (e.g., 30% for **9a**, 140% for **9d**, 100% for **10i** vs the preceramic composites). Physical mixtures of MCM-41 and polymer (**2** and **4**) showed only small increases upon pyrolysis (to **13** and **15**). The large change observed for the pyrolysis of the composites **5** and **7** can be best explained by the presence of monomers/polymers *inside* the channels of MCM-41 prior to pyrolysis. Upon pyrolysis, much of the organic material present inside the channels is lost as volatile species, leaving the Fe nanoparticles.

There is compelling evidence that the Fe nanoparticles are *inside* the channels of MCM-41. First, comparison of the PXRD results for the composites, ceramics, and controls suggests that the polymer is inside the channels. Second, TEM images show Fe nanoparticles inside the host. Only samples which were known to contain excess monomer showed residual ceramic on the exterior surfaces of the particles. Third, we attempted to obtain the Fe and Si distribution in samples from high-resolution TEM line scans across the channels of the microtomed host. Scans showed that the Fe was inside the channels, but the sample decomposed under the electron beam before we could obtain a suitable signal-to-noise ratio to distinguish silica of the channel walls from iron in the interior of the channels. Finally, XPS



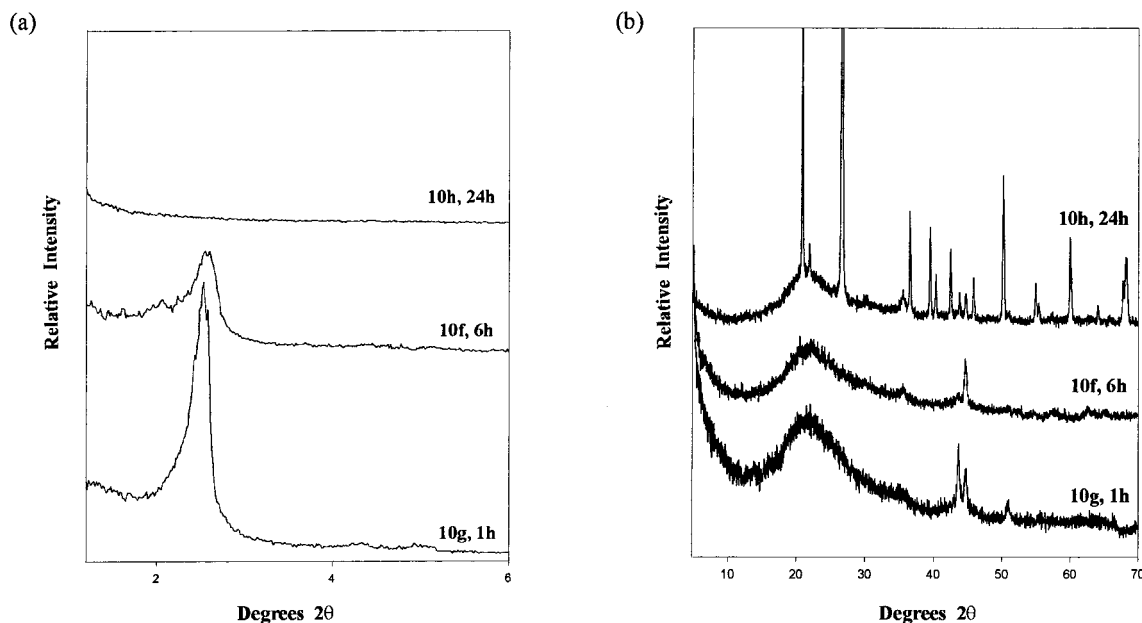


Figure 8. PXRD patterns for ceramics **10f–h** formed at 1000 °C at (a) low angles and (b) high angles.

analysis of pyrolyzed samples showed very little, if any, Fe on the surface of the particles.

**Magnetization Measurements.** PXRD of ceramics **9** indicated that the  $\alpha$ -Fe particles are small enough to be superparamagnetic. To further understand the magnetic properties of these materials, we examined ceramics **9b–d** by superconducting quantum interference device (SQUID) magnetometry. There are several experimental criteria that are used to determine if a sample contains superparamagnetic particles.<sup>6</sup> The temperature-dependent magnetization will exhibit a cusp at the blocking temperature ( $T_b$ ) in the zero-field-cooled (ZFC) magnetization. When cooled in the absence of a magnetic field (zero-field cooling), the magnetic moments will initially be spatially locked in random orientations. If a weak external magnetic field is then applied, the moments may slowly align (Boltzmann equilibration) and will remain aligned until the temperature is increased above  $T_b$ . Above  $T_b$ , the thermal energy overwhelms the ordering effect of the magnetic field and the net magnetization of the sample decreases. Thus, the magnetization curves will display hysteresis below  $T_b$ , but no hysteresis above  $T_b$ . Finally, the plots of  $M$  versus  $H/T$  should superimpose in the superparamagnetic regime.

Figure 9 shows the temperature-dependent magnetization data for the zero-field-cooled susceptibility of **9b–d**. All of the samples show cusps in their ZFC magnetization curves, with maxima ( $T_b$ ) centered at ca. 30 K for **9b** and **9c**, and ca. 45 K for **9d**.

Field-dependent magnetization data were obtained for **9b**, **9c**, and **9d** at several temperatures. Figure 10 shows magnetization curves for **9c**. While hysteresis was not observed at room temperature, the materials all showed hysteresis below 40 K. Sample **9b** showed essentially the same magnetization data as **9c**.

The absence of room-temperature hysteresis in the magnetization curves indicated that the particles were superparamagnetic and the magnetization should be described by the Langevin equation (eq 1). In a distribution of particle sizes, the low-field component of the Langevin function is primarily affected by large particles, while the high-field component is most sensitive to the small particles in the system.<sup>6</sup> The magnetization data for the superparamagnetic materials were fitted to a Langevin

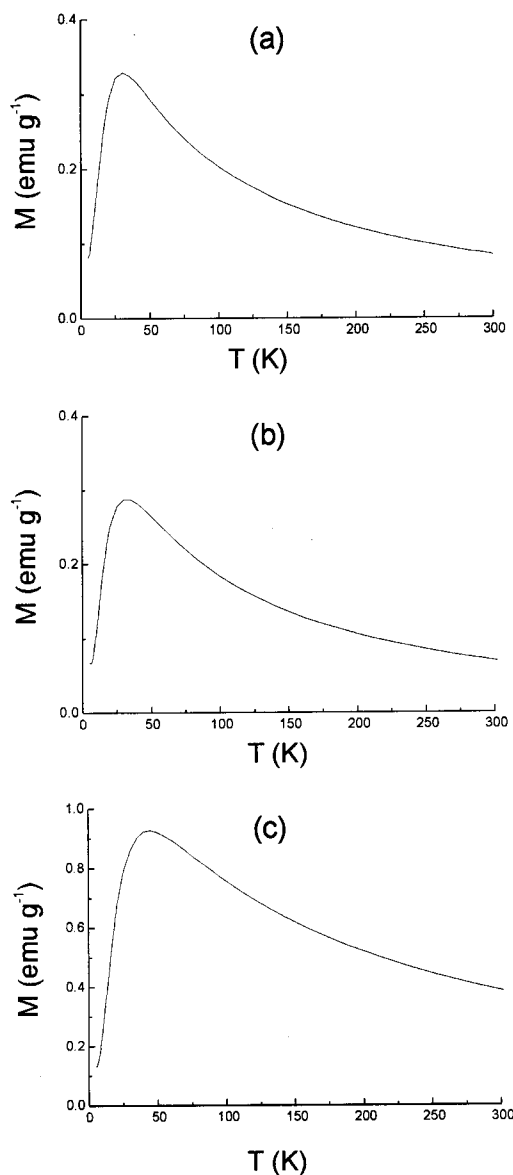
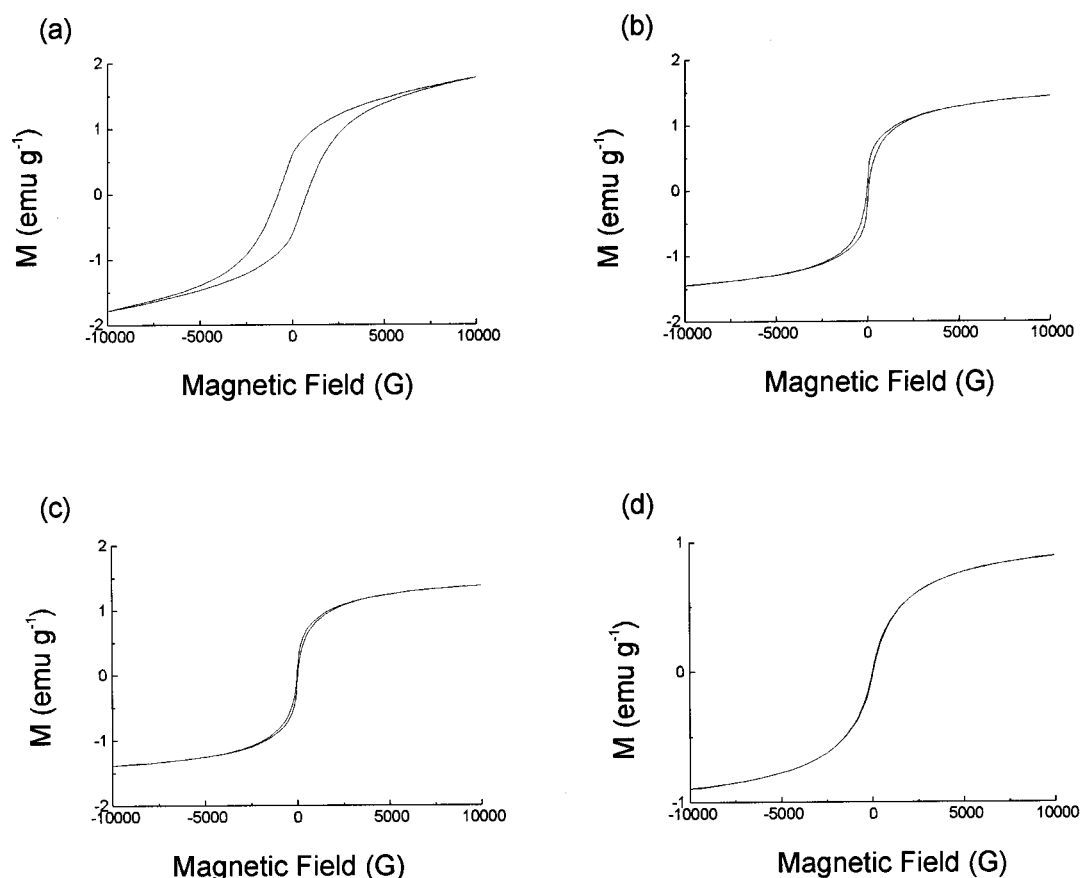


Figure 9. Zero-field-cooling curves of (a) **9b**, (b) **9c**, and (c) **9d** at 100 G.



**Figure 10.** Isothermal magnetization curves of ceramic **9c** at (a) 5 K, (b) 25 K, (c) 40 K, and (d) 300 K.

function assuming that the particles were essentially monodisperse within the channels. As the data fit poorly to a single Langevin function, the data were fitted to a sum of two Langevin functions (eq 2). Honda et al. have used this equation in their treatment of Fe nanoparticles in alumina and silica substrates.<sup>35</sup> This modification of the Langevin function is reasonable when a bimodal distribution of grain sizes is present, or when particles of two magnetic materials are present.

Essential approximations, which may not necessarily be valid, were made during data analysis. First, the particles were assumed to be precisely bimodal and spherical, and to possess isotropic magnetization. However, the inherent geometry of the silica channels, the iron–silica anchoring, and the iron structure may introduce a degree of magnetic anisotropy. Second, the particles were assumed to be isolated and non-interacting. The potential contribution to the magnetization from other magnetic phases that may be present in the material (e.g.,  $\text{FeC}_x$ ,  $\text{Fe}_x\text{O}_y$ ,  $\text{FeSi}_x\text{O}_y$ ,  $\text{FeSi}_x$ , and  $\text{FeN}_x$ ) was ignored. Finally, the diamagnetism of the silica and pyrolyzed organosilicon products was assumed to be negligible.

Figure 11 shows the plot of  $M$  vs  $H$  at 300 K along with the components of the Langevin function (eq 2) for ceramic **9c**. Magnetization parameters are summarized in Table 2. Figure 12 illustrates two possible models to explain the bimodal nature of the particle distribution. As only  $\alpha$ -Fe was observed in the PXRD patterns of **9b–d**, it was first assumed that the particles were  $\alpha$ -Fe. From the calculated fit to the bimodal Langevin function (eq 2), the largest Fe particles had diameters 50–64 Å and the smaller particles had diameters 28–36 Å (Table 3).

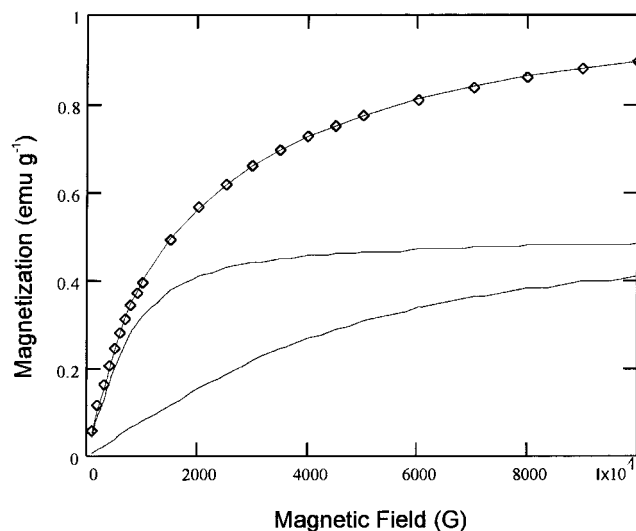


**Figure 11.** Magnetization data for **9c** (at 300 K) fitted to the Langevin function. The upper trace shows the data points ( $\diamond$ ) and the fit curve. The two Langevin components of the fit are shown below.

If a bimodal distribution of Fe nanoparticles is in fact present, the particle sizes approximately represent smaller clusters confined to a single channel (ca. 40 Å) and larger clusters confined to two channels. The latter could form if the ca. 10 Å silica wall between two particles in adjacent channels was disrupted.

More likely, the smaller superparamagnetic contribution arises from an oxide layer on the Fe particles (Figure 12b). If a spherical surface coating of  $\text{Fe}_3\text{O}_4$  (the only oxide phase confirmed in any of our experiments) is assumed, then the particles possess oxide layers that are 4–6 Å in thickness (Table

(35) (a) Sakamoto, I.; Honda, S.; Tanoue, H.; Hayashi, N.; Yamane, H. *Nucl. Instrum. Methods Phys. Res. B* **1999**, *148*, 1039. (b) Honda, S.; Okada, T.; Nawate, M.; Tokumoto, M. *Phys. Rev. B* **1997**, *56*, 14566.

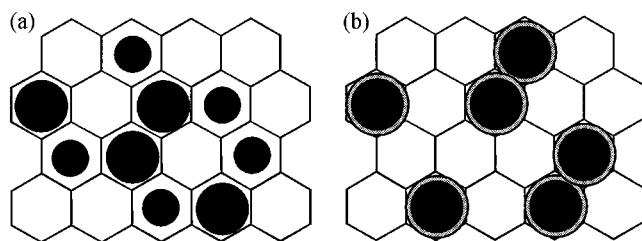


**Figure 12.** Two proposed models to explain the observed magnetization data for magnetic particles in MCM-41: (a) a bimodal distribution of Fe nanoparticles and (b) Fe nanoparticles contained in an iron-silicate shell.

**Table 3.** Fe Particle Sizes and Oxide Thickness

	9b	9c	9d
$D_{\text{mag}}$ (Å) of small Fe particles	28.7(0.4)	28.0(0.5)	36.3(0.5)
$D_{\text{mag}}$ (Å) of large Fe particles	50.9(0.7)	50.0(1.0)	64.4(1.4)
oxide thickness (Å)	4.5(0.8)	4.4(1.0)	5.8(1.4)

3). This oxide layer could constitute the Fe–SiO<sub>2</sub> interface between the nanoparticles and the channel wall. Other researchers have noted that magnetic particle sizes ( $D_{\text{mag}}$ ) may overestimate the particle size measured by TEM by up to 40% due most likely to particle interactions.<sup>7e</sup> Thus, the Fe nanoparticles for **9b,c** ( $D_{\text{mag}} \sim 50$  Å in diameter) may actually be confined to a single channel (diameter of  $\sim 40$  Å). There are clearly larger particles present in **9d** that could form by merging images of particles in adjacent channels of MCM-41. These results are in agreement with the data obtained from PXRD (Table 4).

The magnetization behavior of samples **9b** and **9c** was remarkably similar, suggesting that the choice of host silica affected the magnetic particles obtained from the pyrolysis. Moreover, the calculated particle sizes for **9b,c** were smaller than those for **9d**, agreeing with the observation of a lower

**Table 4.** Comparison of Fe Particle Sizes Determined by PXRD and Magnetization

	9b	9c	9d
Fe particle size from PXRD (Å) <sup>a</sup>	28(2)	31(2)	41(5)
Fe particle size from magnetization (Å)	50.9(0.7)	50.0(1.0)	64.4(1.4)
channel diameter from PXRD (Å) <sup>b</sup>	47	48	38

<sup>a</sup> From Scherrer equation. <sup>b</sup> This is calculated from  $a_0 = 2d_{100}/\sqrt{3}$  for a hexagonal lattice. Note that the quoted channel diameter does not take into account the width of the silica wall.

blocking temperature by ZFC magnetization measurements for **9b,c**. The particle sizes calculated from the Langevin function are consistent with the relative blocking temperatures and particle sizes calculated from PXRD for **9b–d**.

## Conclusions

This paper presents the synthesis and characterization of a novel class of superparamagnetic nanostructured ceramics. The use of ring-opened poly(ferrocenylsilanes) as precursors to Fe-containing ceramics inside mesoporous silica represents a new synthetic strategy to this class of magnetic materials, which may be a candidate for applications that require nanoscopic metal particles.

**Acknowledgment.** We thank the Natural Sciences and Engineering Research Council of Canada (NSERC) for financial support of this research, for a postgraduate scholarship (1995–1999, M.J.M.), and for an E. W. R. Steacie Fellowship (1997–1999, I.M.). G.A.O. acknowledges the Killam Foundation for the award of an Isaac Walton Killam research fellowship (1995–1997). I.M. thanks the University of Toronto for a McLean Fellowship (1997–2003) and the Ontario Government for a PREA Award (1999–2004).

JA992006Y